HIGH RESOLUTION OPTICAL COHERENCE TOMOGRAPHY (OCT) SYSTEM FOR INTEGRATION WITH A MULTIMODAL OPTICAL IMAGING WORKSTATION

by

KAPIL BHARATI LANGER

Presented to the Faculty of the Graduate School of

The University of Texas at Arlington and

The University of Texas Southwestern Medical Center at Dallas

in Partial Fulfillment of the Requirements

for the Degree of

MASTER OF SCIENCE IN BIOMEDICAL ENGINEERING

THE UNIVERSITY OF TEXAS AT ARLINGTON

May 2006

ACKNOWLEDGEMENTS

To Dr. Digant Dave, thank you for the opportunity to work on such an interesting project. Your guidance helped me obtain a greater understanding of optics and instrumentation. For this appreciation and understanding, I am grateful.

To Dr. Hanli Liu and Dr Khosrow Behbehani, thank you for your support, guidance and advice during my graduate studies, your help led me to this outstanding project. Thank you.

To my parents, thank you for all your support throughout my life. You always encouraged me to follow my dreams.

To my brothers Akshay and Arvind without whose support and encouragement none of this would have been possible.

I would also like to extend my special gratitude to Manish and Rakhee for all the moral support and technical expertise that they provided during the crucial phase of my thesis.

November 14, 2005

ABSTRACT

HIGH RESOLUTION OPTICAL COHERENCE TOMOGRAPHY (OCT) SYSTEM FOR INTEGRATION WITH A MULTIMODAL OPTICAL IMAGING WORKSTATION

Publication No. _____

Kapil Bharati Langer, MS.

The University of Texas at Arlington and
The University of Texas Southwestern Medical Center at Dallas, 2006

Supervising Professor: Dr Digant Dave.

Development and construction of a high resolution Optical Coherence Tomography (OCT) system is described. OCT is one of the modalities in an integrated multimode optical imaging workstation built around an inverted Differential Interference Contrast (DIC) microscope in our laboratory, to image cells and tissue samples. The design and construction of the OCT sample path is dictated by its integration to the optical imaging workstation. The OCT system is controlled via a DAC card, interfaced using LabVIEW to the computer. The image of the sample under observation is constructed from the raster scan data acquired by the DAQ. Ti-Sapphire broadband laser source provides the input to the interferometer. OCT resolution being

highly dependent on the bandwidth of the source, the effect of bandwidth on depth resolution is experimentally evaluated and it is seen that the depth resolution increases with increase in bandwidth. Sample path for enface scan and reference path for depth scan is calibrated and tested. Dispersion compensation is performed. SNR for the system is experimentally measured to be 61dB. Experiments showing high resolution imaging capability with variety of samples are demonstrated.

TABLE OF CONTENTS

LIST OF ILLUSTRATIONS

Figure Page

LIST OF TABLES

Table Page

CHAPTER 1

INTRODUCTION

1.1 Background

Optical Coherence Tomography (OCT) is an optical imaging technology widely used in the field of biomedical engineering. OCT can be seen as modality very similar to ultrasound, where backscattered light is measured instead sound. OCT provides high resolution depth resolved images of samples under investigation [1]. This modality uses the backscattered light from the sample to investigate the internal microstructures of the sample. Closely spaced lateral depth scans are used to generate a virtual 2D slice of the sample [1].

The noninvasive property of this technique makes it an important modality for diagnostic imaging [2]. OCT is intensively used in imaging the tissue in the eye [3][4-8]. OCT as an imaging modality has also being successful in imaging highly scattering media such as tissue and skin [9][3][10][11]. This modality has found its way into MEMS, devices and probes have been developed for in vivo application [3][12][13][14]. OCT's capability of providing high resolution morphological information of tissue under investigation has made it very popular among researchers working towards cancer detection [12][15][10][16]. Many improvements in the areas such as image acquisition speed, penetration depth, resolution for this modality have been made over the years, but the basic principle has stayed the same. Light from NIR laser splits into sample and reference path of the Michelson's interferometer. The

interferometer also recombines the light coming back from the sample and the reference path into one signal. An interferometer signal is then detected when the path length of the light in both the arms of the interferometer are matched. OCT performs multiple scans as the sample under investigation is scanned by the laser.

1.2 Motivation

The OCT system was built as a part of an optical workstation for imaging cells and tissue sections. The idea of incorporating multiple imaging modalities to get high resolution tomographical images of tissue samples was the motivation towards building the OCT system. (This system can be considered as the first of the imaging modalities system towards a virtual imaging station for the biomedical optics lab). The OCT system will be aligned and configured with a DIC microscope. It will generate an image of samples showing the morphological features a few millimeters deep into the sample. It's a fast imaging modality to see within the sample, coupled with another imaging modality like multi photon this technique shows a lot of promise for imaging tissue and cells.

1.3 Specific Aims

The primary objective of this thesis was to design a Time Domain Optical Coherence Tomography system and generate a high resolution image from it. This system would then be assembled on a Differential Interference Contrast (DIC) Microscope to obtain images from DIC and OCT systems simultaneously as a part of a virtual biopsy imaging unit.

Specific aims of the project were:

1) Construction of an ultra high resolution Optical Coherence Tomography (OCT) system.
2) Calibration and testing of the ultra high resolution system
3) Integrating the OCT system with a DIC microscope.

1.4 Organization of this thesis

This section describes OCT as an imaging technique and the motivation towards this thesis. It also lists the specific goals for this thesis.

Chapter 2 describes the OCT setup constructed as a part of this project. This chapter is further sub divided into sections that explain the individual blocks in the OCT set up (Fig 2.1). It also explains the concepts behind the design of the sample path and the reference path of the OCT system.

Chapter 3 describes the software module programmed in LabVIEW to interface the NI 6111 S-series DAQ card. DAQ card is used to provide the input signal to the OCT system and also to acquire the interference signal from the interference set up. This chapter contains the interface design and the flowchart explaining the software modules involved.

Chapter 4 elaborates on the OCT system's performance specifications. Coherence length's dependence on bandwidth is also evaluated. It contains the performance graphs for the sample and the reference path. SNR dependence on intensity and the sample to reference path coupled power ratio is experimentally evaluated.

Chapter 5 contains the OCT images of the samples and discussion related to the images. These images include samples such as mirror and cover slip and also tissue samples such as onion and a human finger.

Chapter 6 is the last chapter of this thesis and it concludes with a discussion of future goals and work for improving the system.

CHAPTER 2

OCT SYSTEM

2.1 Introduction

OCT is based on Low-Coherence Interferometery. Fiber based interferometer is shown in figure 2.1. The four arms of the fiber based interferometer are the source arm, the sample path, the reference path and the detector arm.

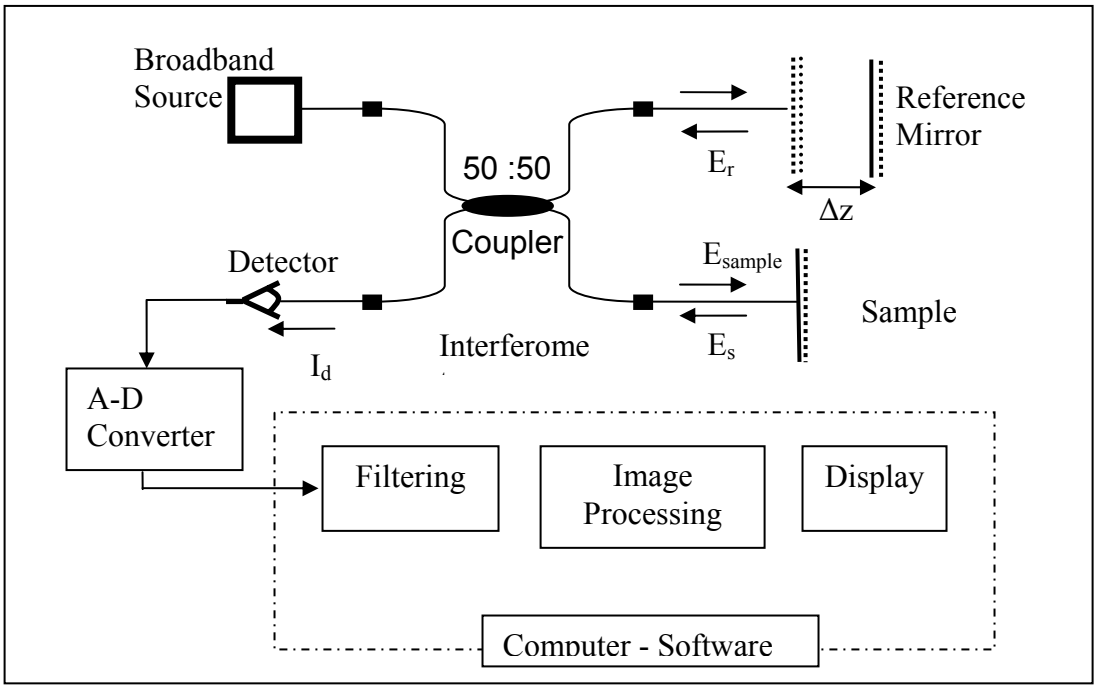

Figure 2.1: Basic block diagram of an OCT setup.

The OCT system comprises of a broad band light source coupled to one of the arms of the interferometer setup. The broadband input to the system is split into the reference field E_r and sample field E_{sample} at the coupler. The beam to the sample path is

focused onto the sample and the back reflected light on the scattered light from the sample which has a field E_s is collected back into the sample path by the scanning optics. The reflected light from the reference arm and the sample arm are detected as combined beams and the intensity at the detector I_d is given as

$$I_d = \langle \left| E_s(t) + E_r(t+\tau) \right|^2 \rangle \tag{1.1}$$

$E_r(t + \tau)$ and $E_s(t)$ are the is the electric field associated with the light coming back from the sample and the reference arms of the interferometer with one beam traveling an extra path length associated with time τ. The cross correlation amplitude is given by integrating the interference signal over the surface of the detector. [1][17][18].The equation 1.1 can be expanded as shown in equation 1.2

$$I_d = \left\langle \left(E_s + E_r\right) \cdot \left(E_s^* + E_r^*\right) \right\rangle \tag{1.2}$$

$$I_d = \left\langle \left|E_r\right|^2 + \left|E_s\right|^2 + \left(E_s \cdot E_r^* + E_r \cdot E_s^*\right) \right\rangle \tag{1.3}$$

writing the irradiance of individual beams as I_r and I_s and using A+A* = 2Re(A)

$$I_d = I_s + I_r + 2\,\mathrm{Re}\left\langle E_s(t) \cdot E_r^*(t+\tau) \right\rangle \tag{1.4}$$

from this it can be seen that if the two beams have the same polarization states the dot product maximizes $\left\langle E_s(t) \cdot E_r^*(t+\tau) \right\rangle = \left\langle E_r(t) \cdot E_s^*(t+\tau) \right\rangle$. Defining normalized correlation function as $\gamma = \left\langle E_s(t) \cdot E_r^*(t+\tau) \right\rangle / \sqrt{I_s I_r}$ we get

$$I_d = I_s + I_r + 2\sqrt{I_s I_r}\,\mathrm{Re}\left[\gamma(\tau)\right] \tag{1.5}$$

from statistical optics we know that the correlation function γ_{12} can be expressed as

$$\gamma(\tau) = \int_0^\infty S(\upsilon) \exp(-i2\pi\upsilon\tau)\, d\upsilon \qquad 1.6$$

$S(\upsilon)$ is the normalized power spectral density of the source. From equation 1.6 we can see that interference pattern would become narrower with the increase in source bandwidth. Form the equation 1.6 we can also say that the correlation functions will be Gaussian for a Gaussian spectrum. The correlation function contributes to the Gaussian envelope to the amplitude modulated interference fringe signal. Figure 2.2 shows the Full Width at Half Maxima (FWHM) and the Maximum and minimum intensity levels for the fringe signal.

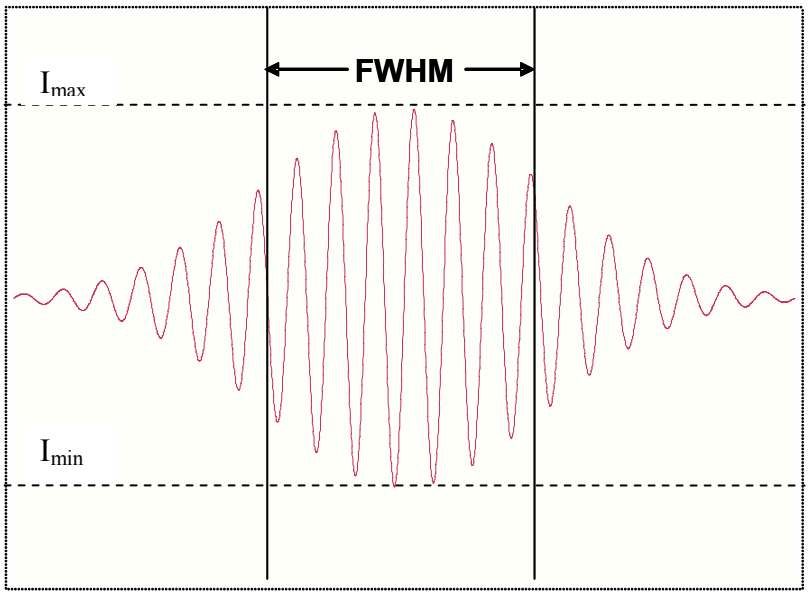

Figure 2.2: Interference fringe signal showing Full Width Half Maxima (FWHM) and the maximum and minimum intensity levels.

The range $I_{max} - I_{min}$ give the range of intensity on the image generated. The range is the maximum when the irradiance from the reference path and the sample path is the same.

The relation between coherence length l_c of the source and the bandwidth $\Delta\lambda$ for a Gaussian source is given as shown in equation 1.4. [1][2][19]

$$l_c = \frac{2c\ln 2}{\pi}\frac{1}{\Delta\nu} = \frac{2\ln 2}{\pi}\frac{\lambda_0^2}{\Delta\lambda} \approx 0.44\frac{\lambda_0^2}{\Delta\lambda} \qquad 1.4$$

The resolution of the OCT system is defined the depth resolution and the lateral resolution of the system. The depth resolution is dependent on the coherence length and the lateral resolution depends on the beam waist on the sample. In OCT, the depth (axial) and the lateral resolutions are independent of one another. Optical axial resolution can thus be increased by selecting a broad band source since the coherence length of the light source is inversely proportional to the bandwidth as can be seen from equation 1.4[2][20].

The numerical aperture (NA) of the lens that focuses the beam on the sample determines the lateral resolution. The lateral resolution for a beam is given as

$$\Delta x = \frac{4\lambda}{\pi}\left(\frac{f}{d}\right) \qquad 1.5$$

where Δx is the beam waist, λ is the wavelength of light used, f is the focal length of the objective and d is the beam diameter at the lens. The depth of focus b is given as

$$b = \frac{\pi\left(\Delta x^2\right)}{2\lambda} \qquad 1.6$$

Equations 1.5 and 1.6 are derived using Gaussian beam optics equations. (An objective with high NA would result in a smaller depth of focus (DOF) as compared to a lens with lower NA. A compromise needs to be found between the lateral resolution and the available DOF [2] [21]).

2.2 Time Domain -OCT Setup

The OCT system comprises of a Ti-Sapphire broad band source which provides mode locked laser at 800nm. The laser is coupled into a fiber based interferometer. The XY scanning optic, delay line and the detector comprise the other three arms of the interferometer.

The beam is directed into a 50:50 optical coupler using an XY-Z stage coupling assembly. The optical coupler splits the beam into the reference arm and the sample arm.

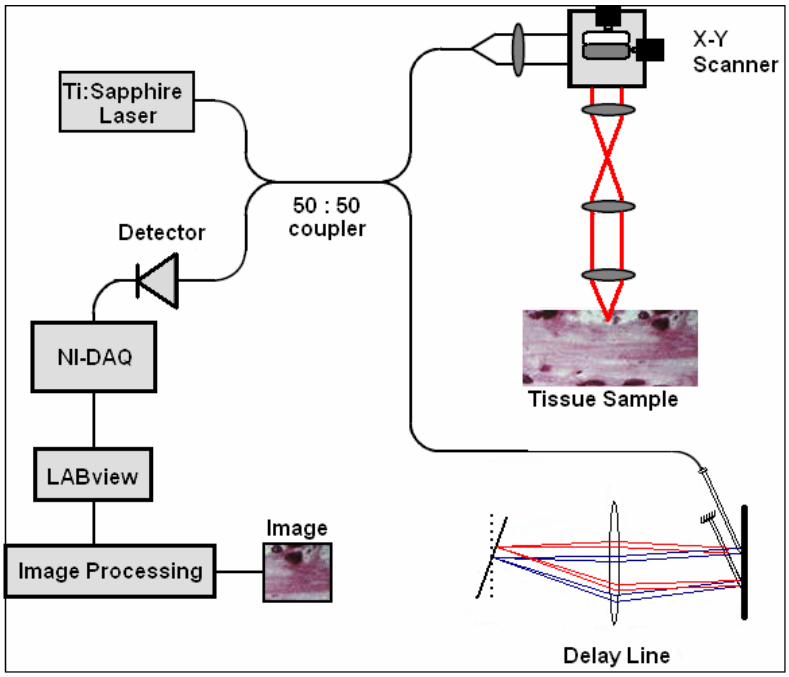

Figure 2.3: Schematic block diagram of the TD-OCT setup.

The reflected light from the reference arm (delay line) double pass setup [22][23][24][25] and the sample is coupled back into the setup. The interference fringes are generated when the path lengths of the reference arm and the sample path are

matched within the coherence length of the source [26]. The fringe signal is detected as amplitude modulated waveform [21] [25].

2.3 Source and Coupler Assembly

The laser source used for the OCT setup is a broad band laser source capable of lasing within the wavelength range of 700nm – 1100nm. A green pump laser as shown in the figure 2.4 is used to pump the broadband Infrared laser.

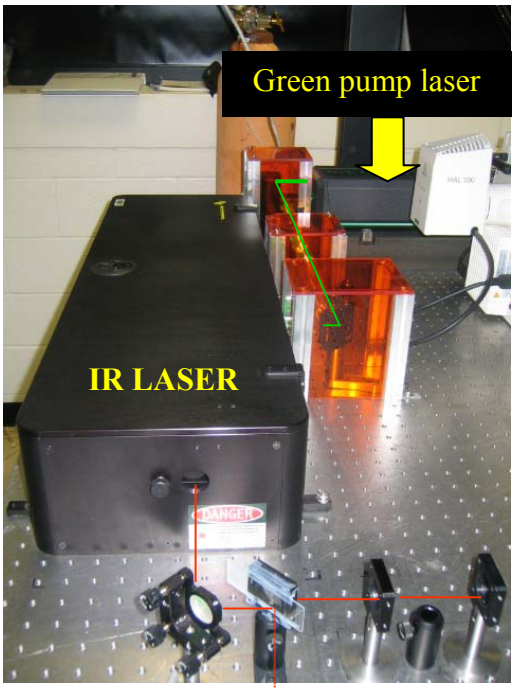

Figure 2.4: Green pump laser and the IR laser source.

The broad band Ti-Sapphire laser source is used at center wavelength of 800nm. This beam is then reflected using a mirror on a tip and tilt stage to couple it into a fiber coupler. A part of this beam is coupled into the spectrometer to check the spectrum of the laser source as seen in the figure 2.5.

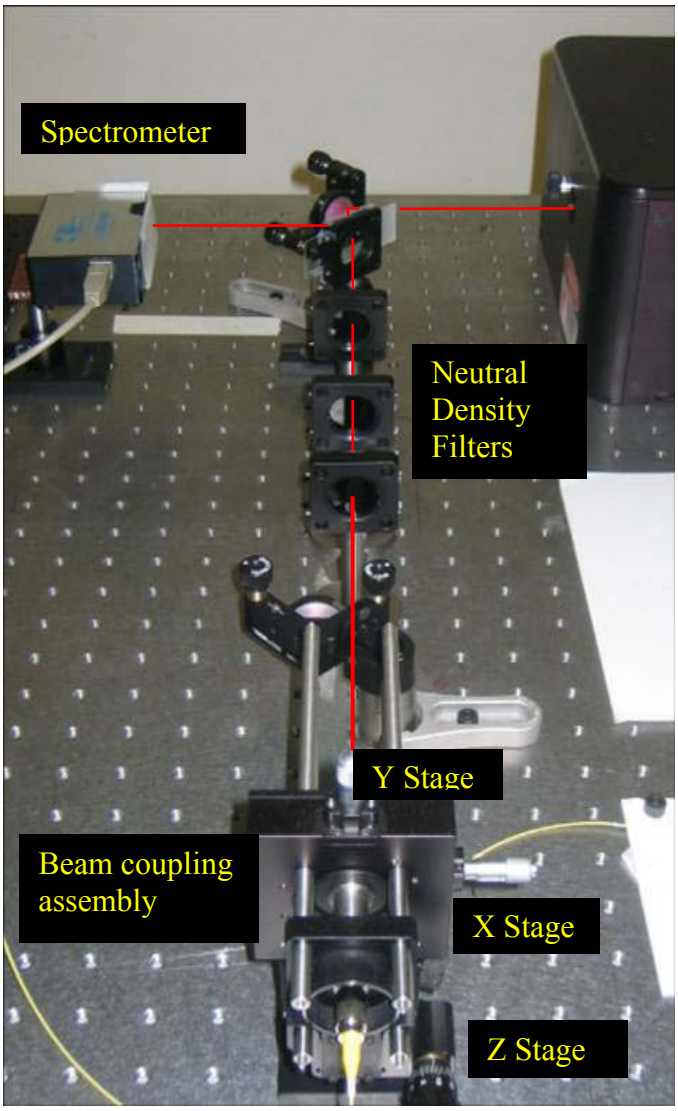

Figure 2.5: The optical set up for the source, spectrometer and the optical coupler.

This laser beam is coupled into a 50:50 optical coupler by the beam coupling assembly as can be seen in the figure 2.5. Beam is focused into the fiber as seen in the figure 2.6.

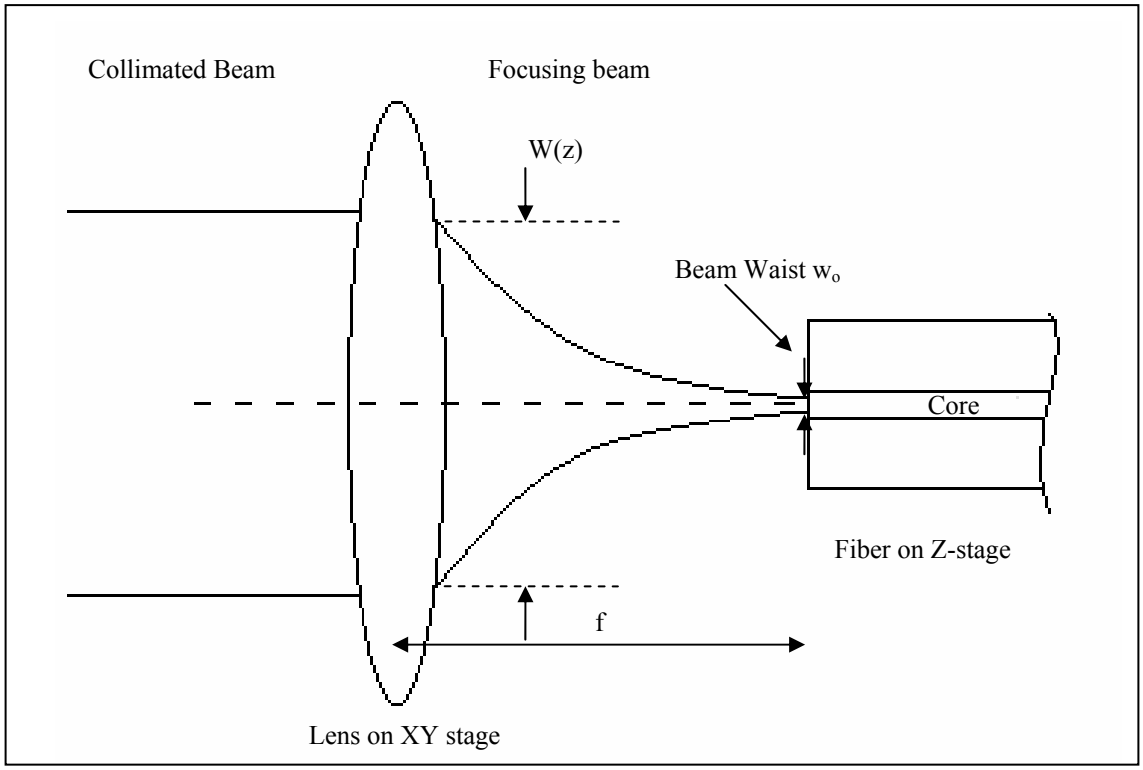

Figure 2.6: XY-Z Fiber coupling assembly schematic diagram.

The beam waist is calculated using the Gaussian beam optics. Based on the equation

$$W(z) = w_0 \left[1 + \left(\frac{\lambda z}{\pi w_0} \right)^2 \right]^{1/2} \qquad 2.1$$

where $W(z)$ is the width of the beam at a distance z , w_0 is the beam waist and λ is the center wavelength of the source. For a focused beam as shown in figure 2.3, equation 2.1 changes to

$$W(z) = \frac{\lambda f}{\pi w_0} \qquad 2.2$$

where f is the focal length of the focusing lens. Here the distance z from equation 2.1 is the same as f itself.

2.3 Fiber based Interferometer

Interferometer is a SM750 fiber with a mode field diameter of 5.9μm, coupler that is used to split the light from the laser into the sample path and the reference path. It is a 50:50 coupler and splits the light equally in the two arms of the interferometer connected to the sample and the reference path. The ends of the fiber coupler are FC connecters tapered to prevent any back reflection of light into the interferometer.

2.4 Sample Path Design

The sample path comprises of a collimator, XY Galvo assembly, an optical relay, and a microscope objective. The sample path setup is shown in figure 2.4. This set up is called the cage assembly as all the optical components are mounted on rods. This helps in maintaining a common optical axis for all the components.

The XY galvo assembly has two galvos placed orthogonal to each other. A galvo or galvanometer is an electromechanical voltage sensitive device that deflects the mirror mounted on a shaft in response to the voltage provided to it. These galvos are controlled through a servo board. The signal to drives these galvos is given to a connector on the servo board. The servo board also has points where you can tap the position and velocity signals coming from the galvos.

The servo boards for all the galvos were placed in a servo box. The servo box has three BNC connectors for each board, one for the input signal to drive the galvos and one BNC connector each for the velocity and the position signal in response to the

input signal to the galvo. The servo box with the BNC connectors can be seen in figure 2.7.

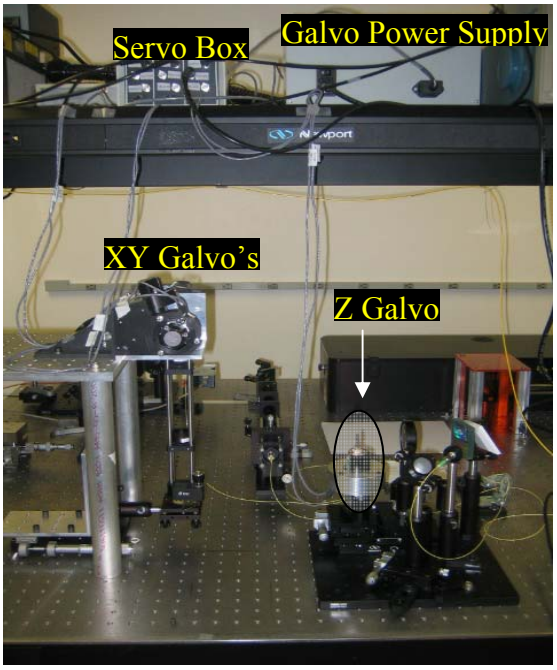

Figure 2.7: The galvos and their controlling instruments.

The power supply to these galvos was provided from an external linear power source. The driving command voltage to the galvos is given through LabVIEW software module through a DAQ interface. The driving signal to these galvos is a triangular wave whose amplitude and frequency depends on the area to be scanned and the type of scan to be performed.

A collimated beam falls on the center of the X Galvo from where it is directed on to the center of the Y Galvo. The Y Galvo directs the beam vertically down to the optical relay assembly comprising of lens *L1* and *L2* as shown in the figure 2.8.

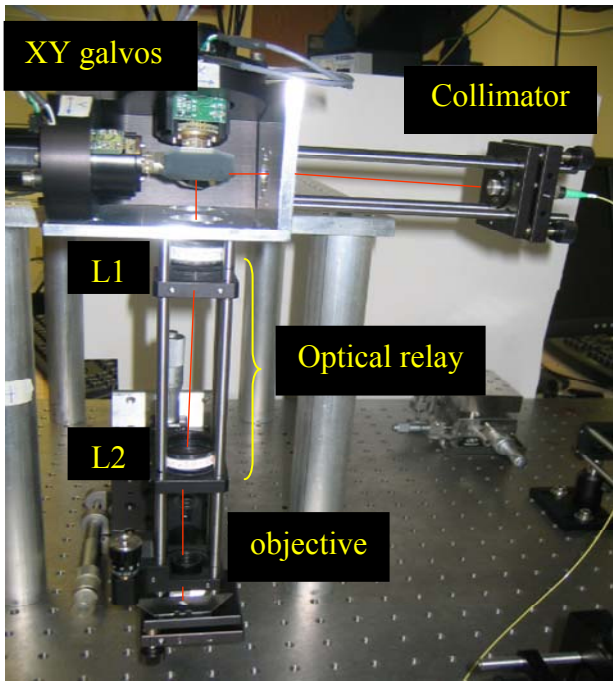

Figure 2.8: Sample path

It is however necessary to align the beam such that it falls at the center of both the Galvo's and comes down after the Y Galvo through the center of the cage system. (This is important to minimize aberrations due to optical elements while scanning and thus optimize the coupling efficiency of the sample path.)

The X and Y Galvos are used to move the focused spot on the sample in X and Y direction respectively. The X galvo is the slow galvo and the Y galvo is the fast galvo. An Enface scan is produced when both the galvo's raster scan the sample as shown in figure 2.8 [27].

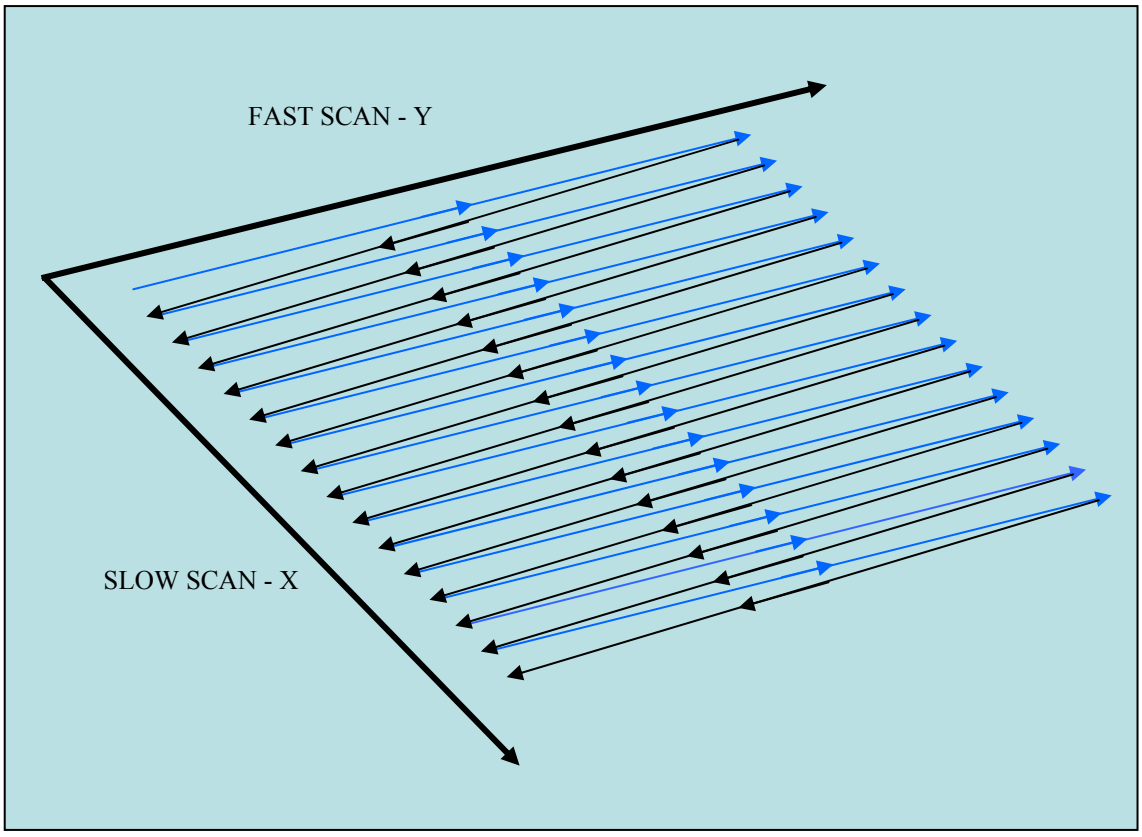

Figure 2.9: 2-D Raster scan performed by reflecting the beam off an XY assembly of the fast and slow moving Galvo's.

Figure 2.10, an elaboration of figure 2.9, explains how the beam traverses on the sample when we move one of the sample path galvos in our setup. The objective focuses the beam spot on the sample. The beam spot on the sample determines the lateral resolution [9] and is given by

$$\Delta r = \frac{2\lambda_o}{\pi NA} = \frac{2\lambda_o f}{\pi \phi}$$

where ϕ is the spot size and NA = $\phi / 2f$

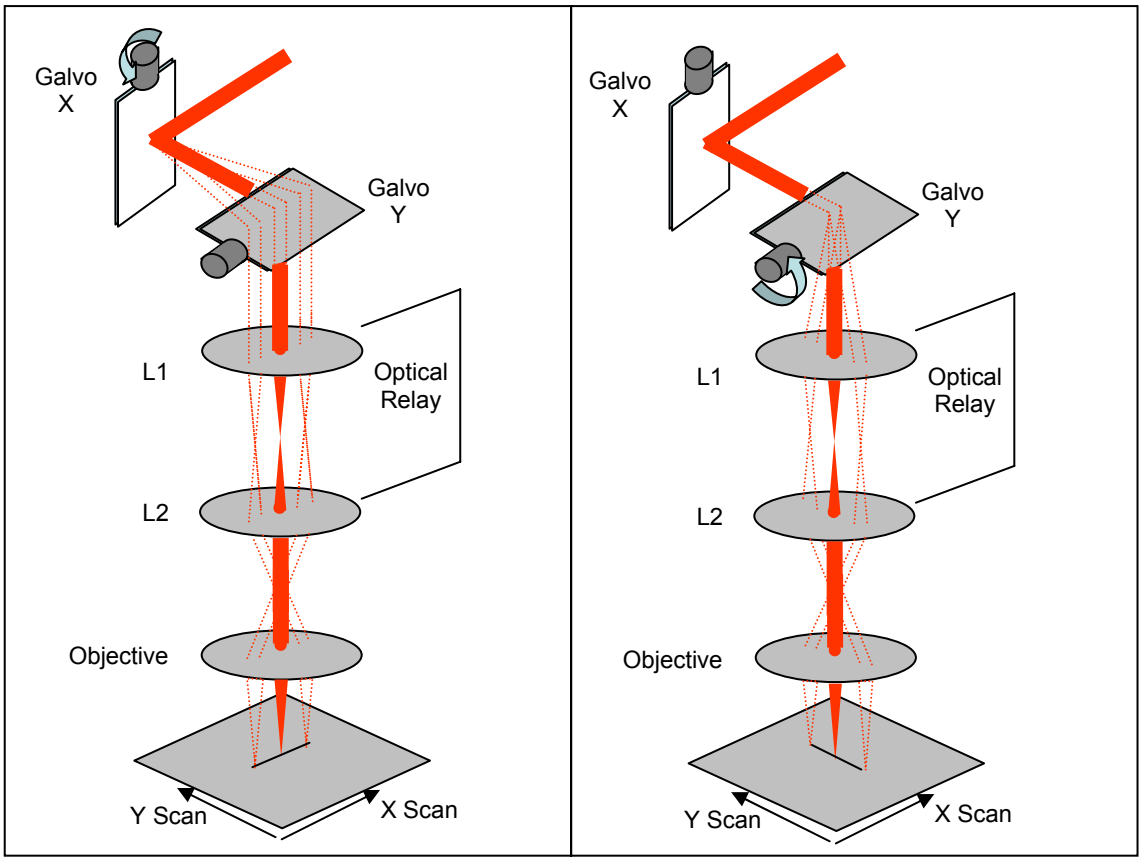

Figure 2.10: Schematic diagram of how the beam scans on the sample in X and in Y direction.

The optical relay shown in the diagram serves the purposes of compensating the path length in the reference arm. The distance between these lenses is critical to get a good focused spot so that we can have good coupling of light back from the sample path. The figure 2.11 below shows the distances between the lenses on the sample path cage assembly.

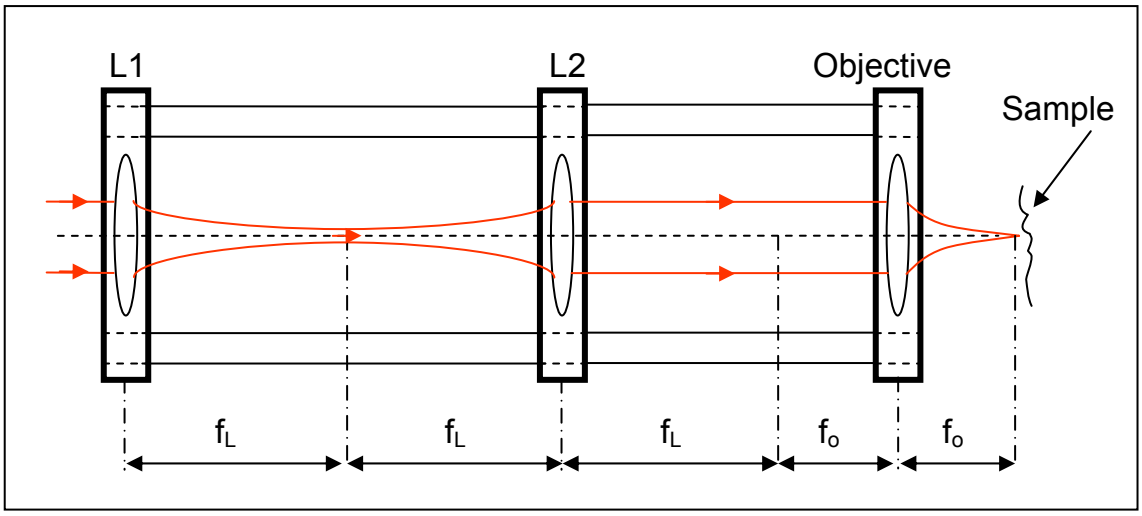

Figure 2.11: The lenses in the sample path with their positions as they are placed.

Lens L1 and L2 are identical and have the same focal length of f_{L1}. The focal length of the objective is f_o. The optical relay makes a parallel beam pass through the back focal point of the objective lens even when the galvo's are scanning as explained in figure 2.10. This will make sure that the beam focuses on the focal plane to give us a better flat field scan on the sample. The back reflected light from the sample is collected by the objective lens with high NA and coupled back to the collimator.

2.5 Reference Path

The delay line set up is a frequency domain optical delay line (FD-ODL) set up which was originally developed for dispersion control and pulse shaping of Pico- and Femto-second pulses [28]. FD-ODL is highly suited for high speed phase- and group delay scanning, making it suitable for the OCT application [22] [29]. Figure 2.12 shows the FD-Optical Delay line set up.

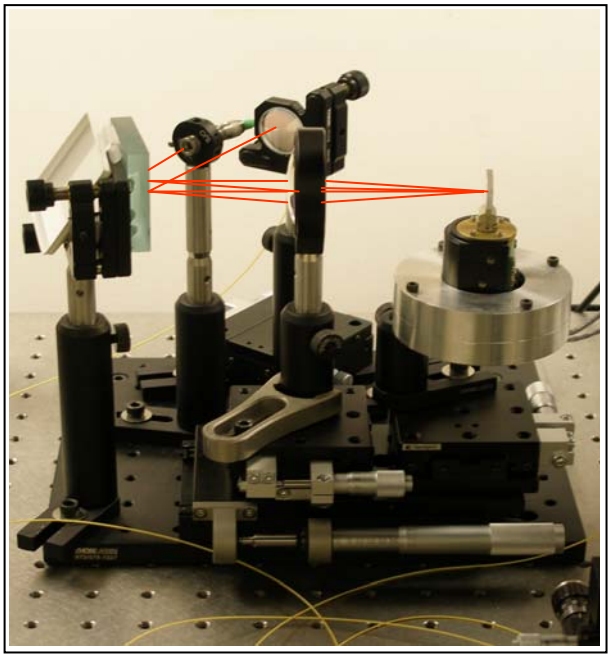

Figure 2.12: Optical delay line.

The delay line setup contains a collimator, a diffraction grating a lens and a galvo. A collimated beam from the collimator falls on the grating and is dispersed among its wavelengths. The dispersed wavelength components get focused on the galvo. The collimator and the grating are aligned in such a way that the mean wavelength component of the broad band source gets diffracted parallel to the optical axis of the lens. The galvo and the lens are located at one focal length away from each other as shown in the figure 2.13. The lens grating distance is varied to compensate for dispersion. The dispersion in the sample path is compensated by the dispersion in the reference path and this compensation will be wavelength and bandwidth dependant.

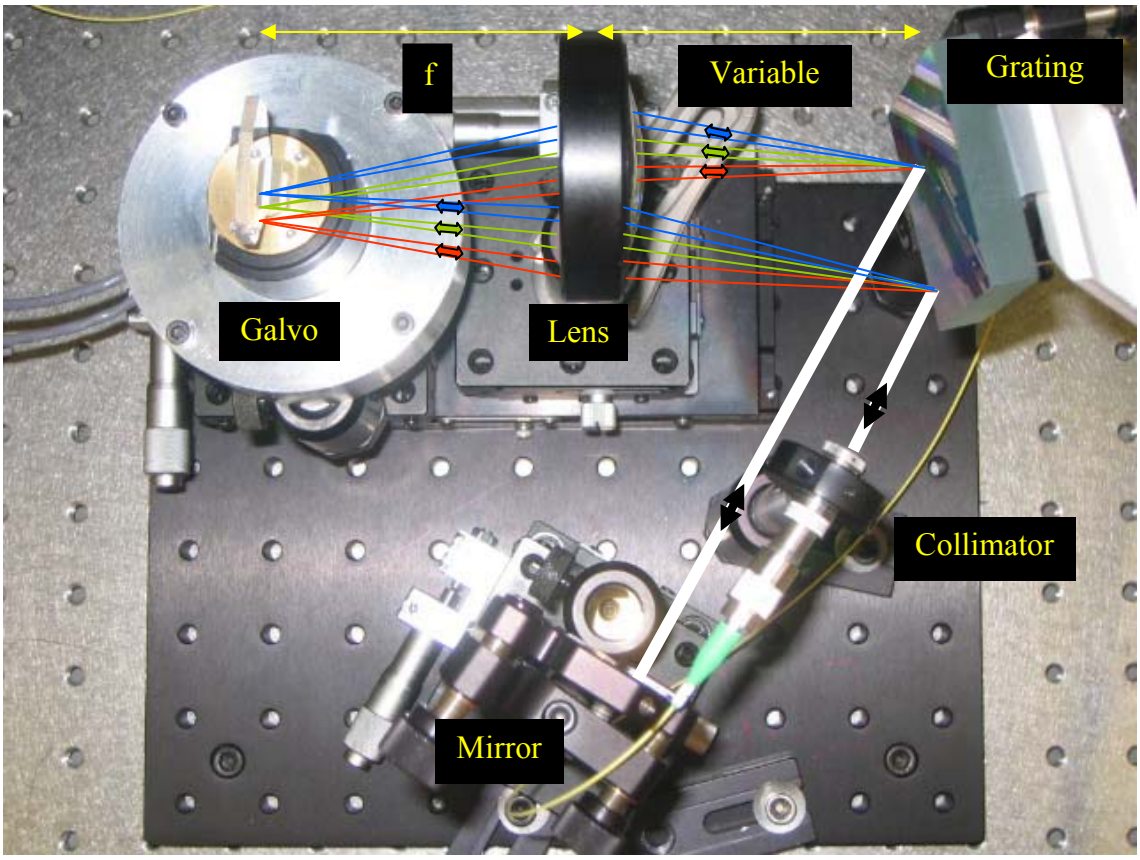

Figure 2.13: Delay line showing how a broad band light gets dispersed into its components and recombines in a double pass setup. The grating to lens and the Galvo to lens distance set to 'f'.

These wavelength components pass through the lens located at a distance of 'f' from the grating. The dispersed wavelength components get focused on the galvo mirror at different laterally displaced positions. The reflected light from the galvo passes through the lens again and the components recombine at the grating. The recombined beam will be laterally displaced and parallel to beam incident on the grating. It is important to get a collimated beam from the grating. The lens to galvo distance can be altered at this stage to obtain a collimated beam. An un-collimated beam can result in loss of wavelength components while recombining the beam back into the collimator. The

recombined beam is reflected from a mirror mounted on a tip and tilt stage for it to retrace its path back in a double pass assembly into the collimator. The light coupled back in collimator is phase modulated by the galvo which moves on a pivot. The reference galvo is controlled externally by a signal generator which also triggers the input to the sample path galvo's. The modulation frequency is a function of galvo frequency and the displacement of the beam on the galvo from the pivot of the galvo. This delay line set up provides depth and phase modulation.

2.6 Detector

Detector path comprises of a high precision amplified silicon detector PDA520. It is a switch able gain silicon detector for detection of light wavelengths in the range of 400 – 1100nm. Detector signal is digitized and collected using a dual-channel 12-bit, 5-MHz DAQ card. Figure 2.14 shows the PDA520 silicon detector used in the setup.

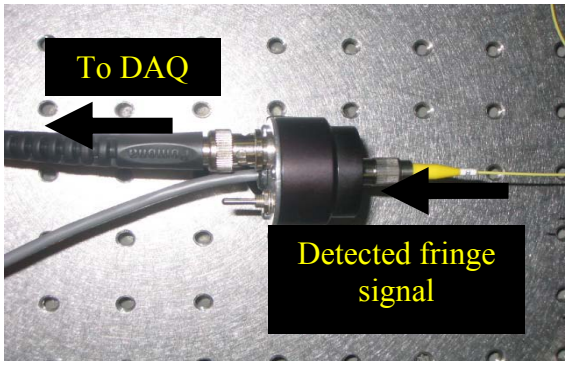

Figure 2.14: PDA 520 silicon detector

CHAPTER 3

LABVIEW INTERFACE

LabVIEW 7.1 a development tool, from NI was used to interface the OCT system with a computer. National Instruments DAQ card 6111 was used to acquire fringe signal from the interferometer. This chapter explains the LabVIEW module designed and programmed to acquire and also to provide the signal for raster scanning the galvo's incorporated in the sample path. There are two VIs, Image Acquisition and Image Display, discussed in this section.

3.1 Interface Design and Flowchart

Software interface for the OCT system is built using LabVIEW virtual instrument (VI). The user should be able to mention the scan area and the type of scan and the software should take care of all the parameters to be provided to the OCT system.

3.2.1 Image Acquisition.

The VI for image acquisition has a sub VI that processes the binary data acquired by the system and displays an Image. The data acquired is stored in the form of a binary file. The figure 3.1 shows the front panel of the VI designed.

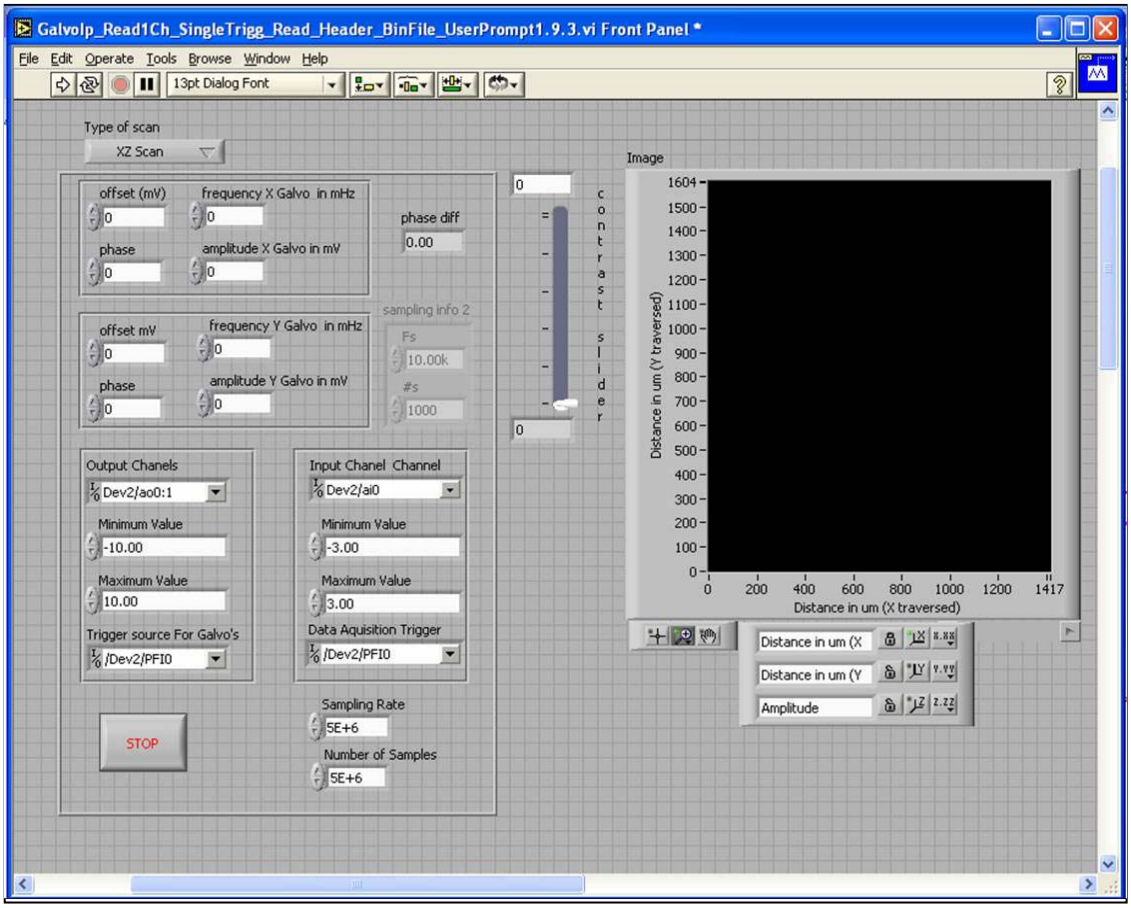

Figure 3.1: The LabVIEW virtual Instrument for characterization of the OCT system.

Figure 3.2 shows the flowchart that explains the flow of control in the VI shown in figure 3.1. The two processes shown in the flowchart are a part image acquisition and display. The process that reads **"Prompt User from Reference Galvo Information and Header file parameters"** pops up a window that requests the user to provide information regarding the scan. This information is logged in as a header to the data file that is acquired. This information is critical for processing the data file to construct an image from the sequentially acquired data.

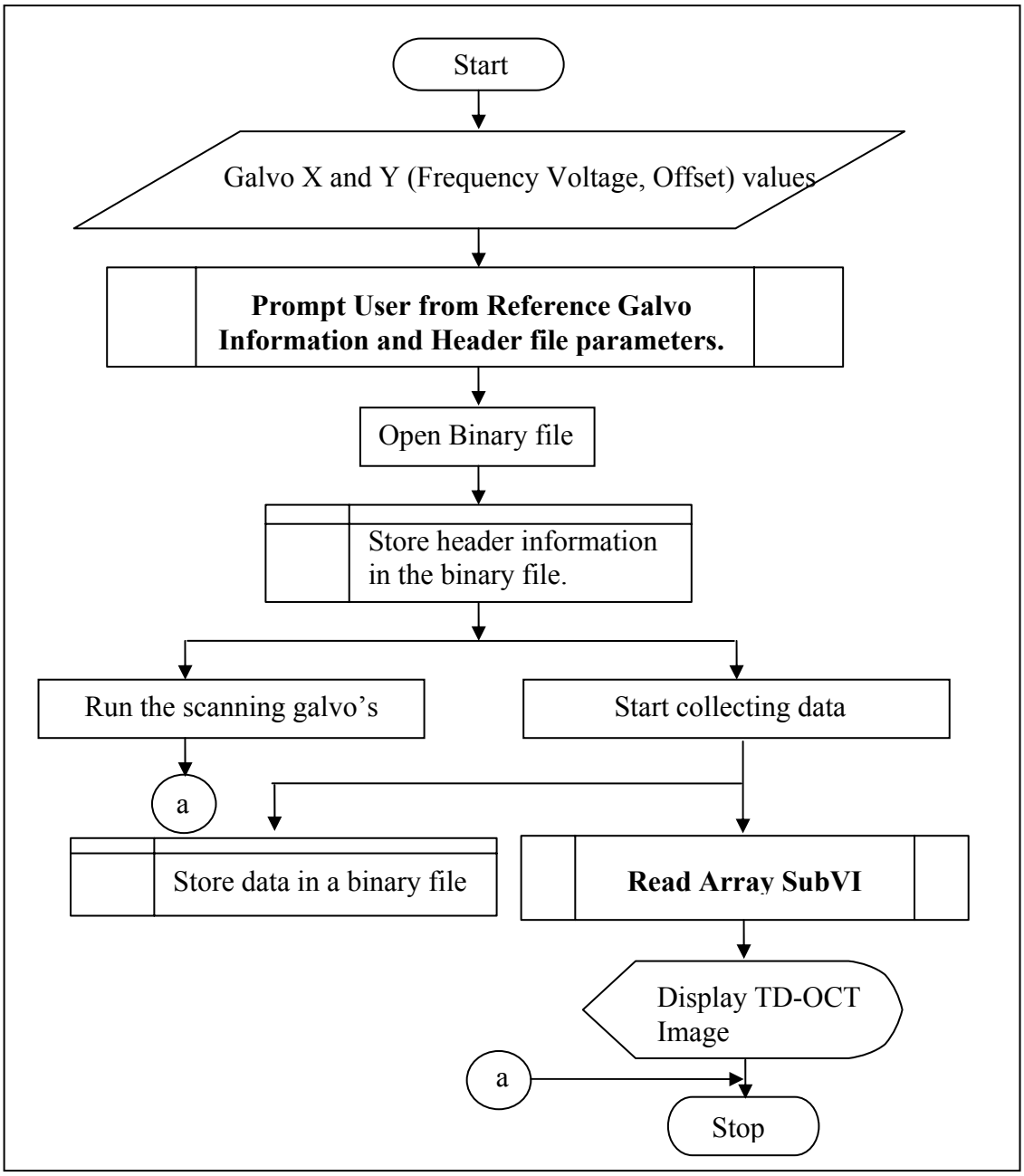

Figure 3.2: Flowchart for Image acquisition, storage and display VI.

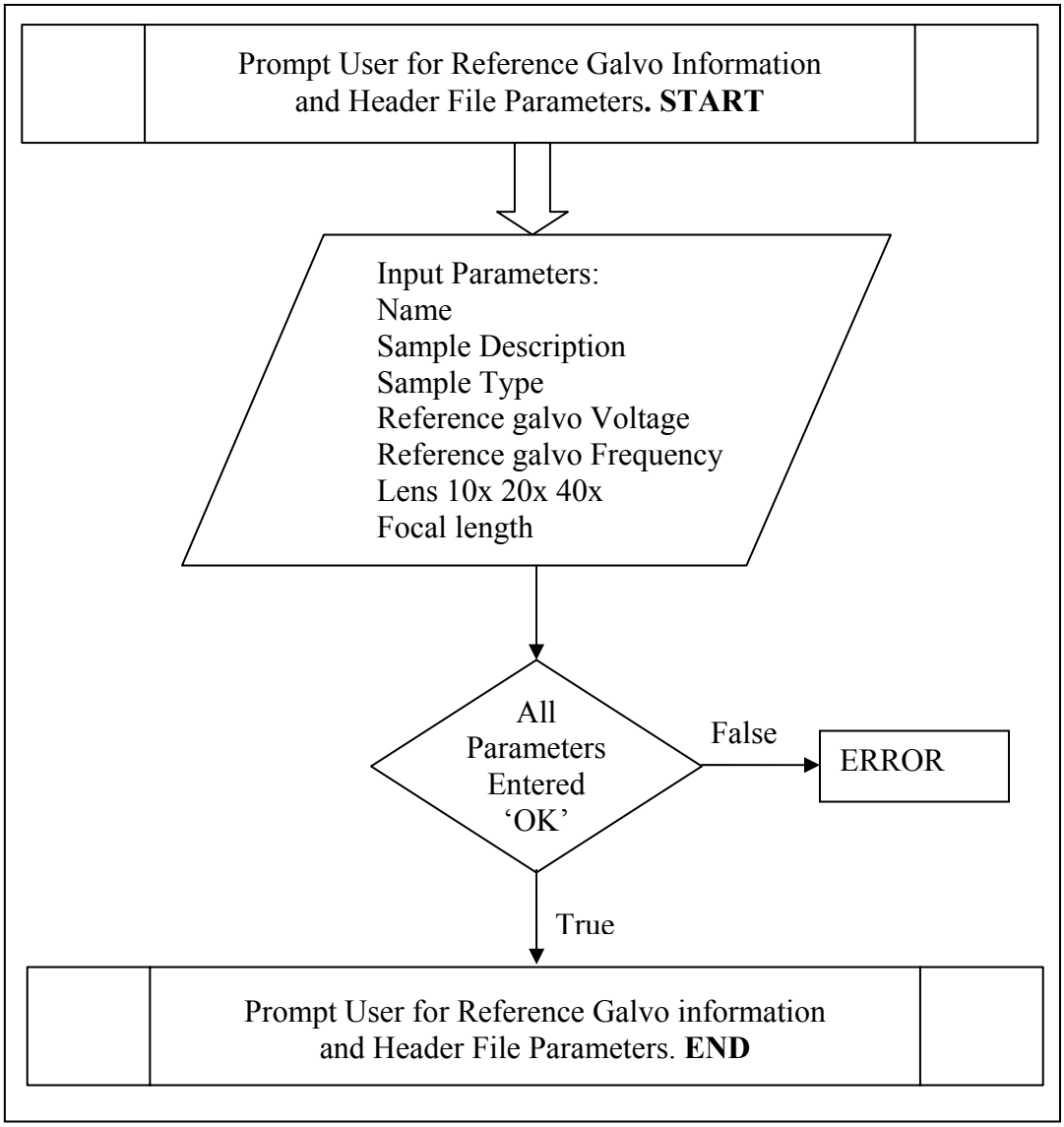

Figure 3.3: Flowchart for Prompt User from Reference Galvo Information and Header file parameters Sub VI.

Second process **"Read Array SubVI"** reads the data acquired by the system. Using the parameters calculated by the characteristics graphs of the sample and the reference paths which are more elaborately discussed in chapter 4, an image is generated.

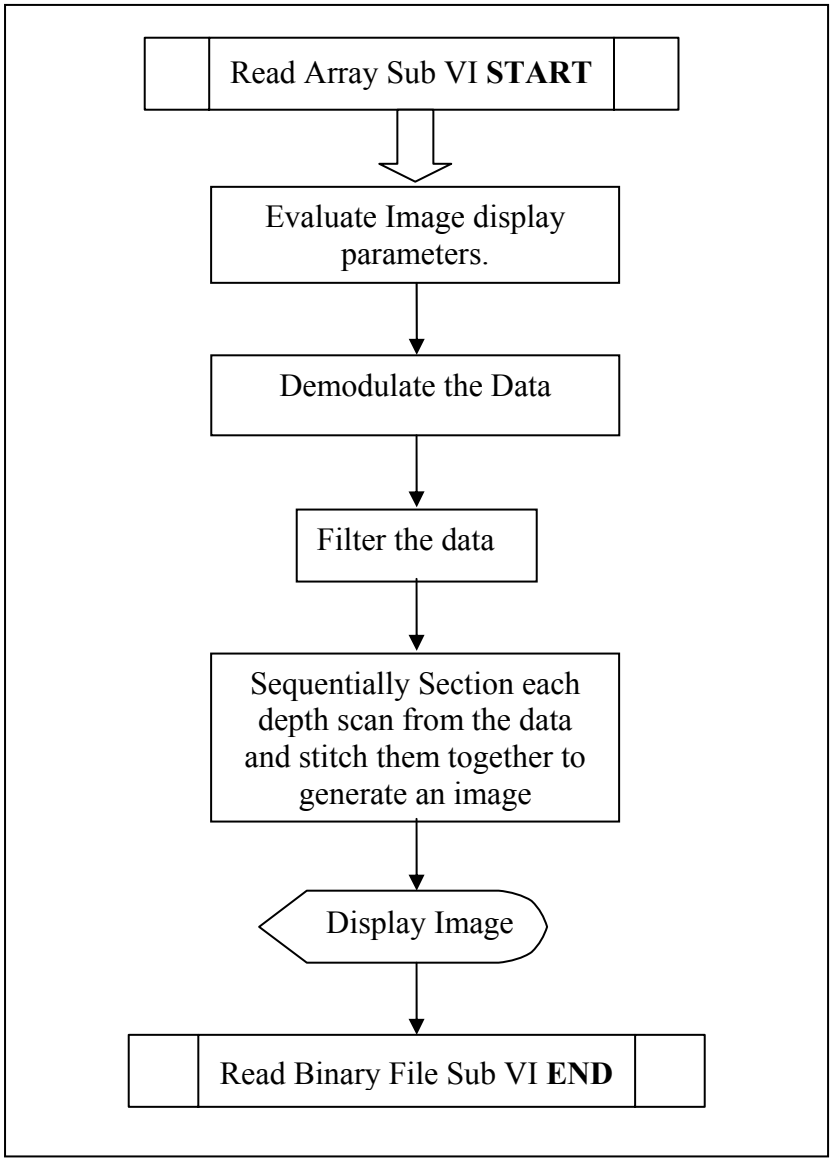

Figure 3.4: Flow chart for Read array Sub VI

The processing involved in the **"Read array SubVI"** is demodulation of an amplitude modulated signal. Data acquired is an amplitude modulated data. The information about the sample lies in the envelope of the AM signal (the information is also there in the fringe frequency but for TD-OCT we only use the envelope). The data

is demodulated and filtered and all depth scans are arranged one next to each other to generate an image. Figure 3.4 shows the control flow for the Read array Sub VI.

3.2.2 Image Display

This module displays the OCT image of the data stored in a binary file format.

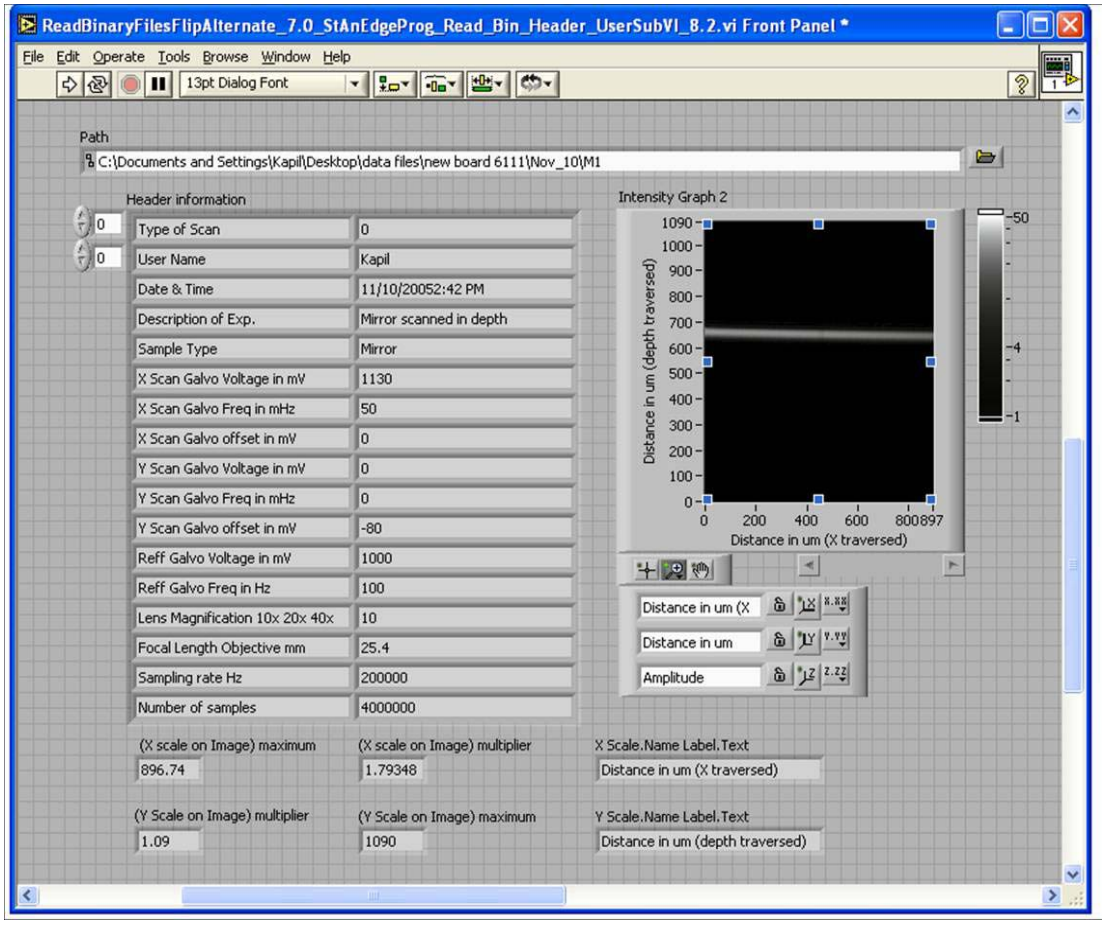

Figure 3.5: LabVIEW Virtual Instrument to read binary data and generate an Image.

Figure 3.5 shows the Virtual Instrument to retrieve the OCT images from binary files saved using the image acquisition VI. This module takes in the data file (Binary File) name to extract the header information using a **"Read header"** Sub VI and displays the image. Figure 3.6 shows the control flow for the VI

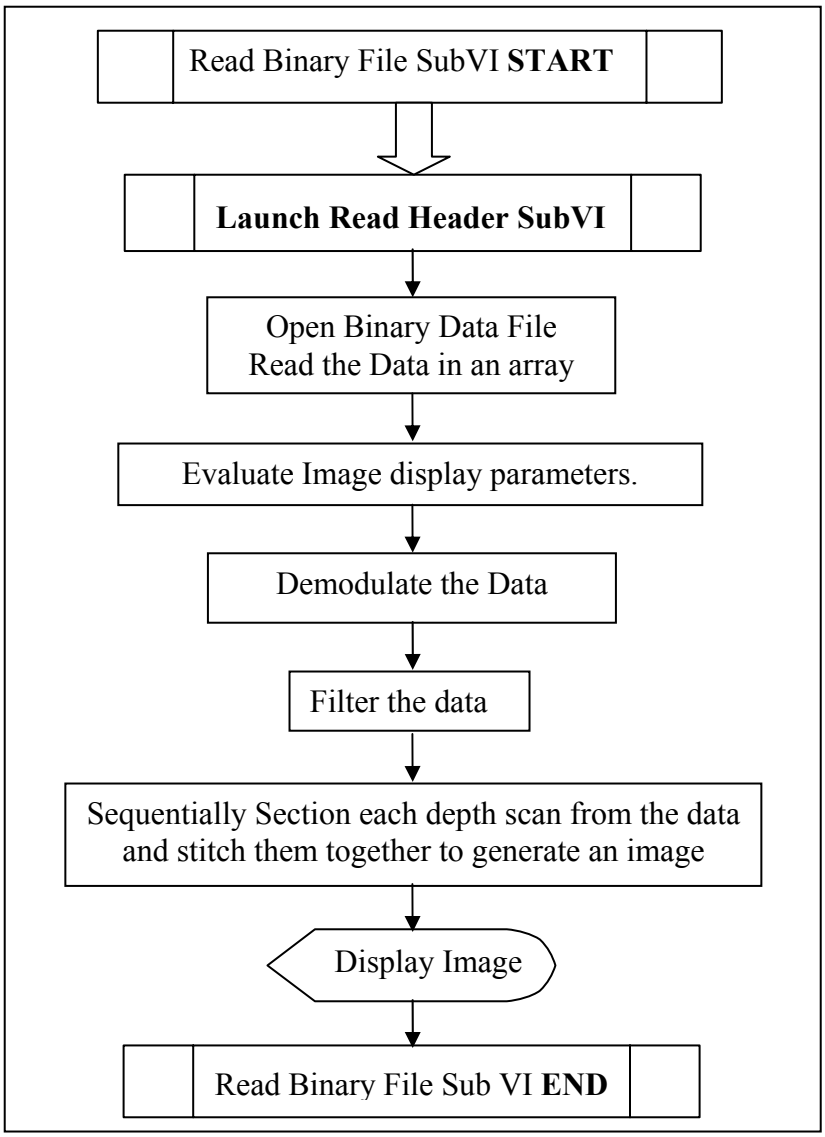

Figure 3.6 Flowchart for binary image file read and displays VI.

Header information is displayed in the front panel. The image acquisition parameters retrieved from the header are used to determine the size, the filter parameters, the scales and the axes of the image and the aspect ratio of the image.

CHAPTER 4

SYSTEM CALIBRATION AND CHARACTERIZATION

4.1 Source

The source used for the OCT system is a Kapteyn-Murnane broad band source capable of a lasing within a range of 700 to 1100 nm. The fringe signal or the detector signal of the interferometer changes with change in the bandwidth of the source. Figure 4.1 shows a typical fringe signal obtained from a single reflector.

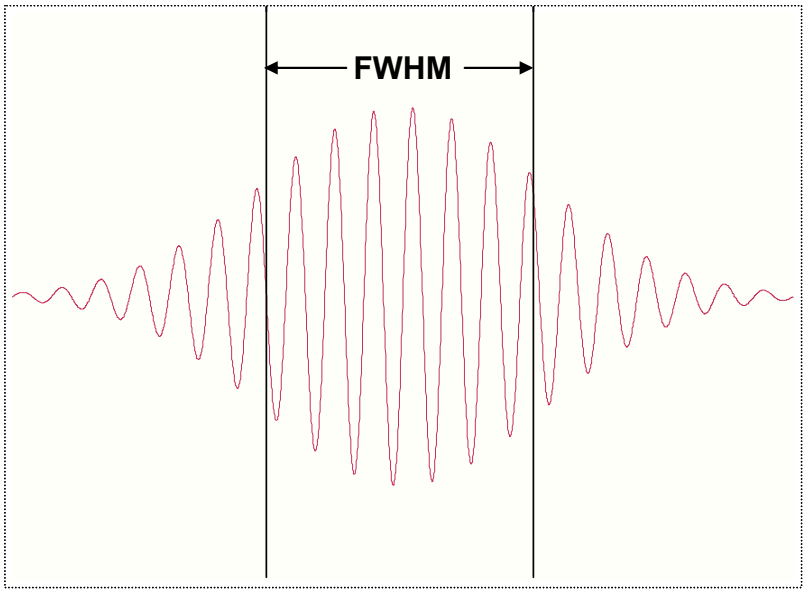

Figure 4.1: Interference fringe signal. Coherence length marked as $L_{c.}$

The FWHM (coherence length) of this signal determines the depth resolution. The FWHM changes with the bandwidth of the source. It increases with decrease in bandwidth resulting in lower depth resolution and it decreases with increase in

bandwidth resulting in a higher depth resolution [30]. Figure 4.2 shows how the coherence length changes with change in bandwidth.

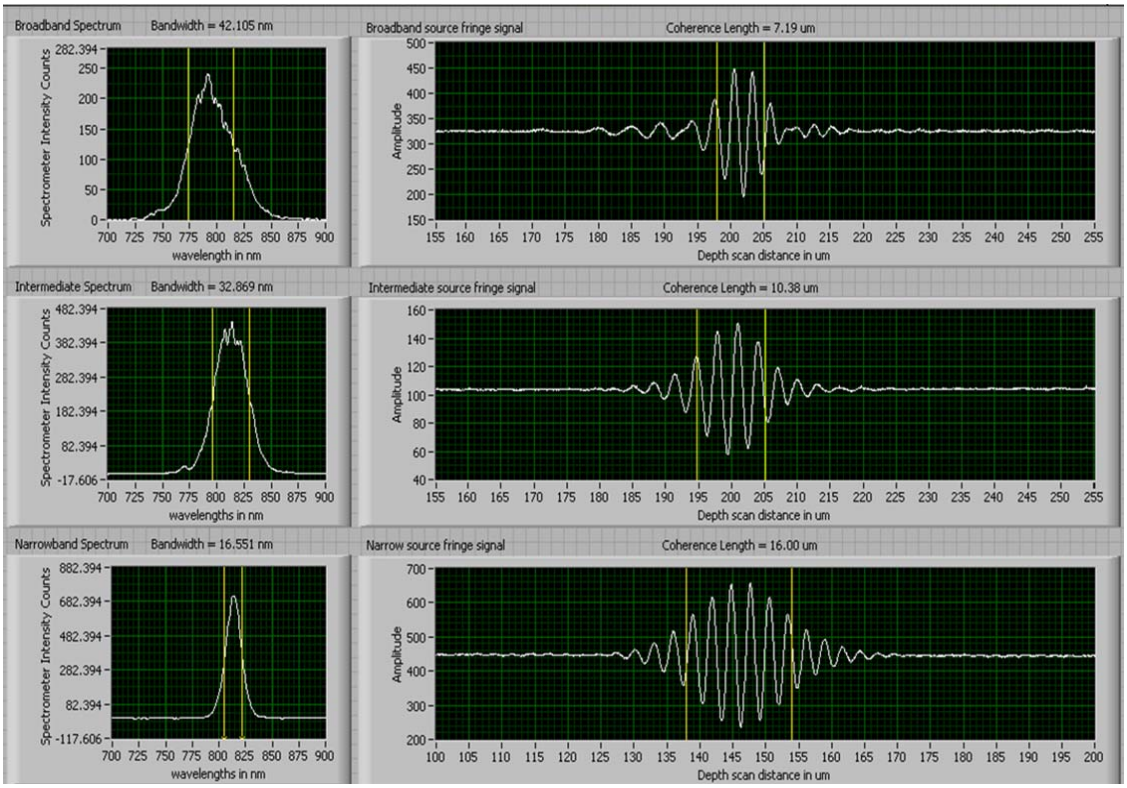

Figure 4.2 Three spectral conditions. Broad band, Intermediate band and Narrow band. Coherence length changes as a function of Bandwidth.

The table 4.1 shows the comparison of theoretical values of coherence length calculated by the spectrum bandwidth using equation 2.4 to the coherence length form the fringes seen for the spectrum. The coherence length increases with increase in bandwidth.

Table 4.1: Comparison of theoretical and experimental coherence lengths.

Spectrum	Bandwidth $\Delta\lambda$ (nm)	L_c from spectrum (theory) (μm)	L_c from fringe (experiment) (μm)
Broadband	42.105	6.687	7.19
Intermediate band	32.869	8.567	10.384
Narrow band	16.551	17.014	16.00

4.2 Sample path

Galvos of the sample path are driven by a triangular wave scan in X and Y direction. Scan distance is dependent on the driving input to the galvos.

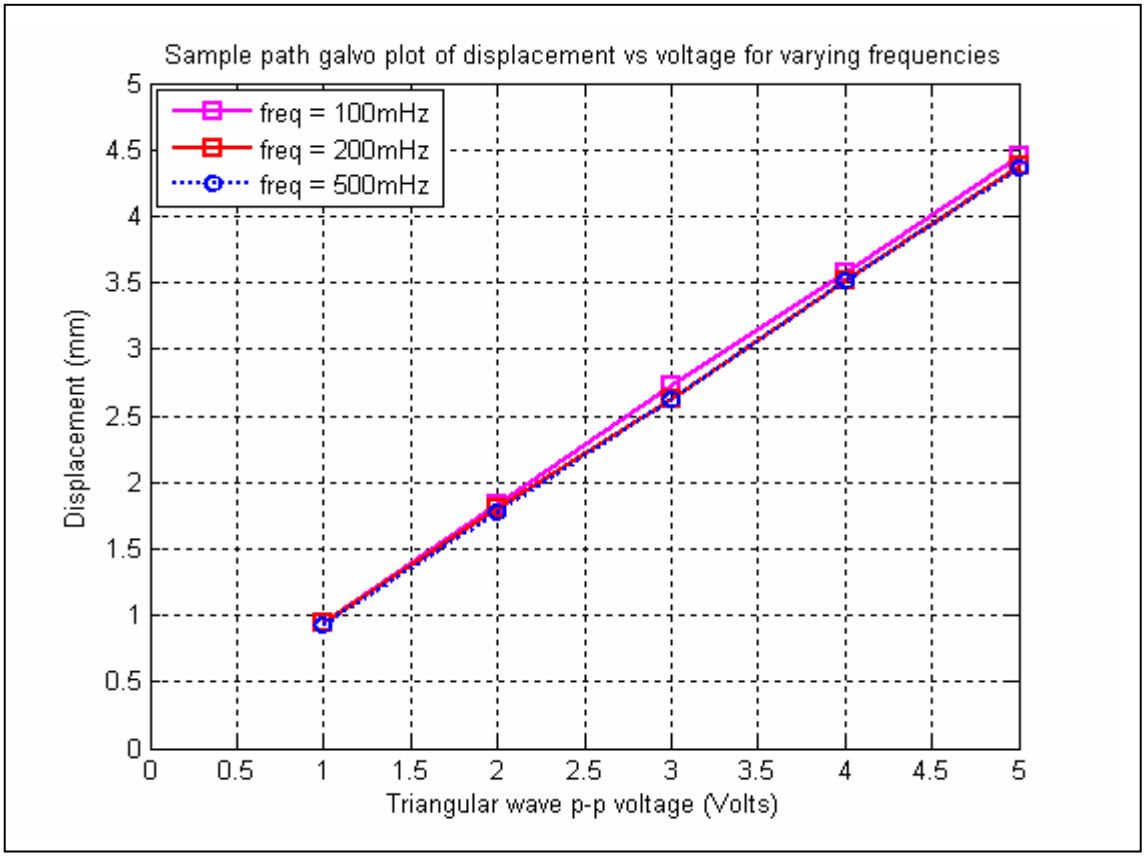

Figure 4.3: Plot of displacement vs. voltage for sample path galvos.

Figure 4.3 plots the scanning galov's displacement as a function of peak to peak input voltage for galvos running at 100 mHz, 200 mHz and 500 mHz.

There is also a frequency dependent delay between the trigger to the galvo and its response. Figure 4.4 plots the time delay between the trigger and the beginning of the scan (i.e. the beginning position is defined as the peak of the position signal from the galvo.).

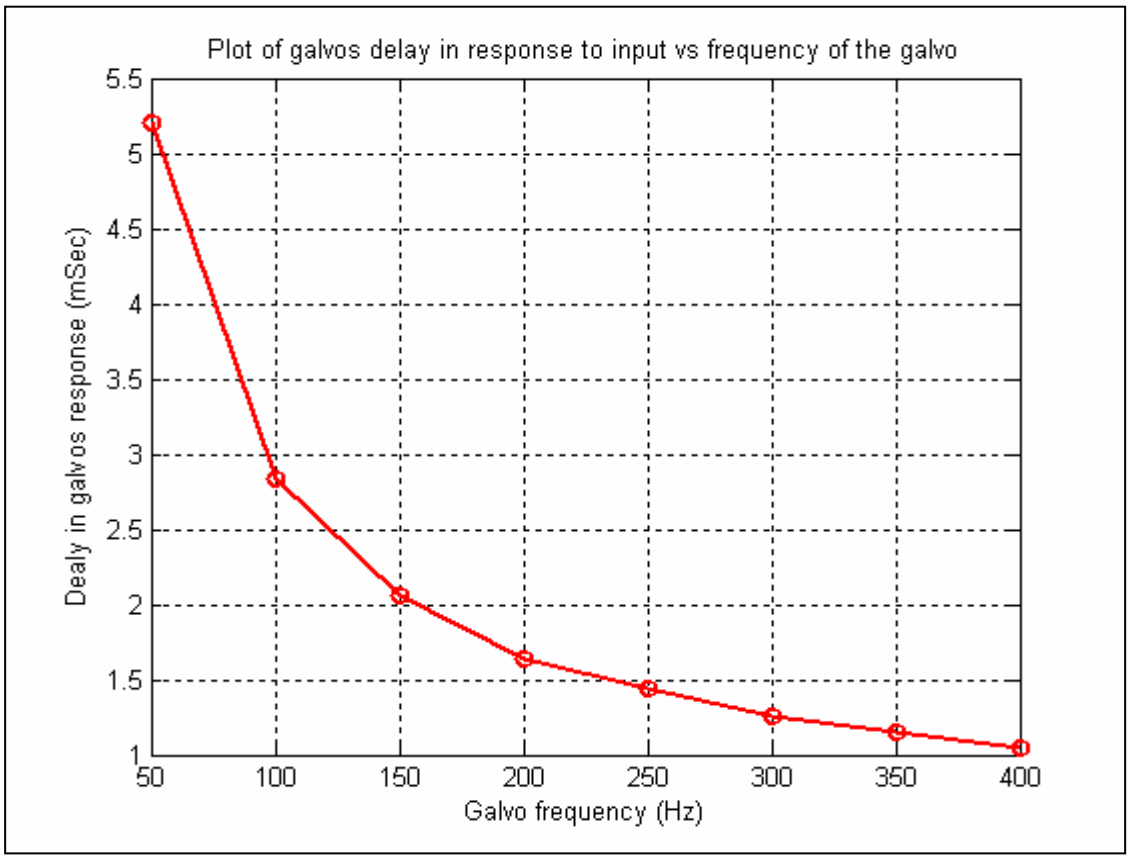

Figure 4.4: Plot of galvos' responses delay to a trigger vs. frequency of the galvo.

The curve of best fit for the data collected for the scanning galvos is a nonlinear 4^{th} order polynomial expression. This expression is used to calculate the time delay between the galvo response and the trigger.

As the galvo go away from their electrical home position while scanning, the coupling of light back into the sample path decreases (the intensity of reflected light being coupled back into the system). Figure 4.5 shows how the intensity drops as a function of scanning distance. The graph shown below is plotted for optimum coupling position.

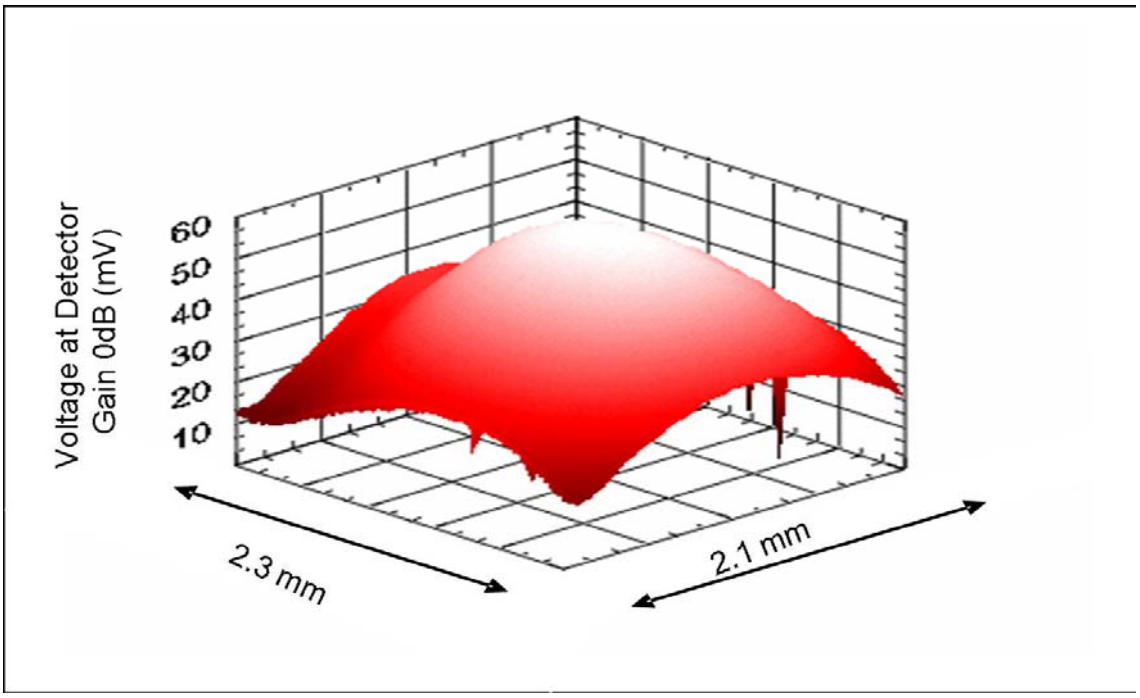

Figure 4.5: Coupling intensity as a function of scan distance in the sample path.

As seen in figure 4.5 the coupling of light back into the system is maximum in the middle (we call it the zero position of the galvo) and fades of gradually as we increase the scan distance.

4.3 Reference path

Reference path comprises of the third galvo of the OCT system. This galvo provides the depth and the phase modulation to the beam in the reference path. The scan depth of the OCT system is dependent on the input signal to the galvo. Figure 4.6 shows the relationship of scan depth to the voltage provided to the reference galvo.

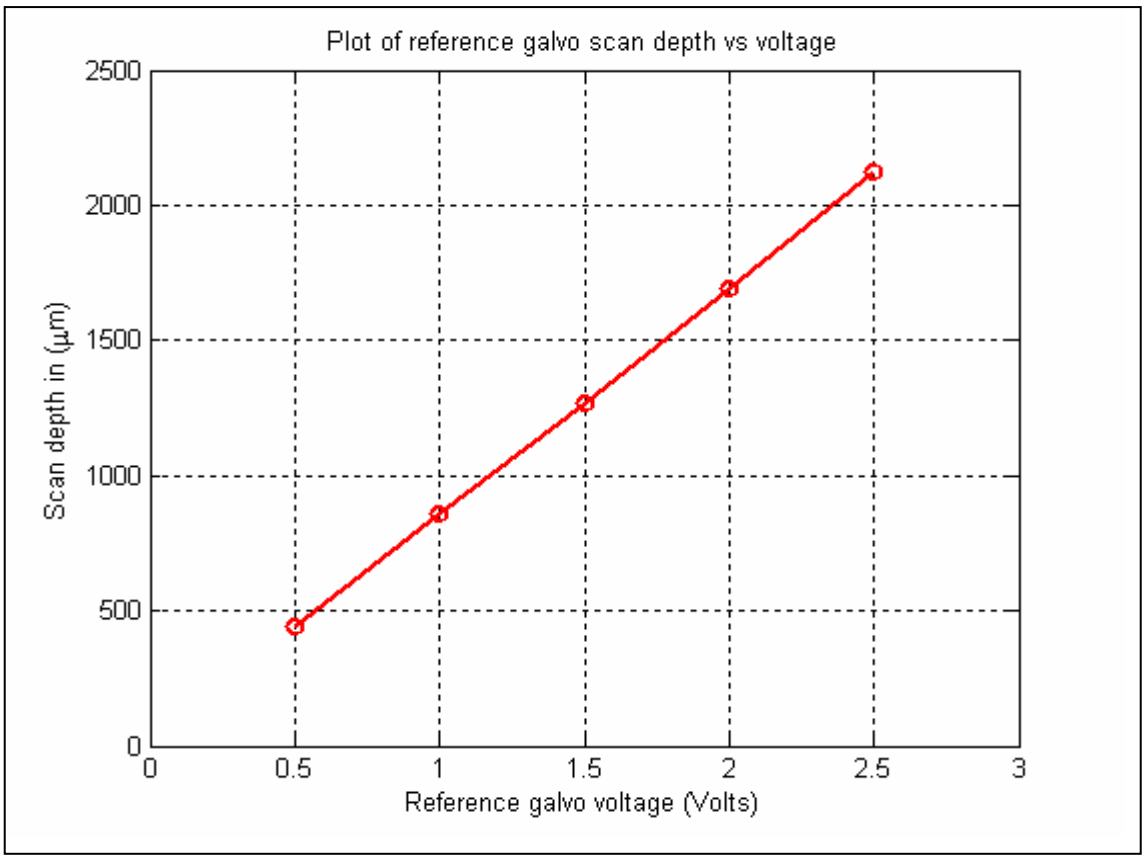

Figure 4.6: Reference galvo scan depth dependence on input voltage.

As the galvo is driven with a larger p-p voltage the modulation in the depth scan also increases. The modulation is given as the ratio of peak to peak AC signal to the DC component of the signal. Scan modulation is linearly proportional to the command voltage driving the depth galvo as shown in figure 4.8.

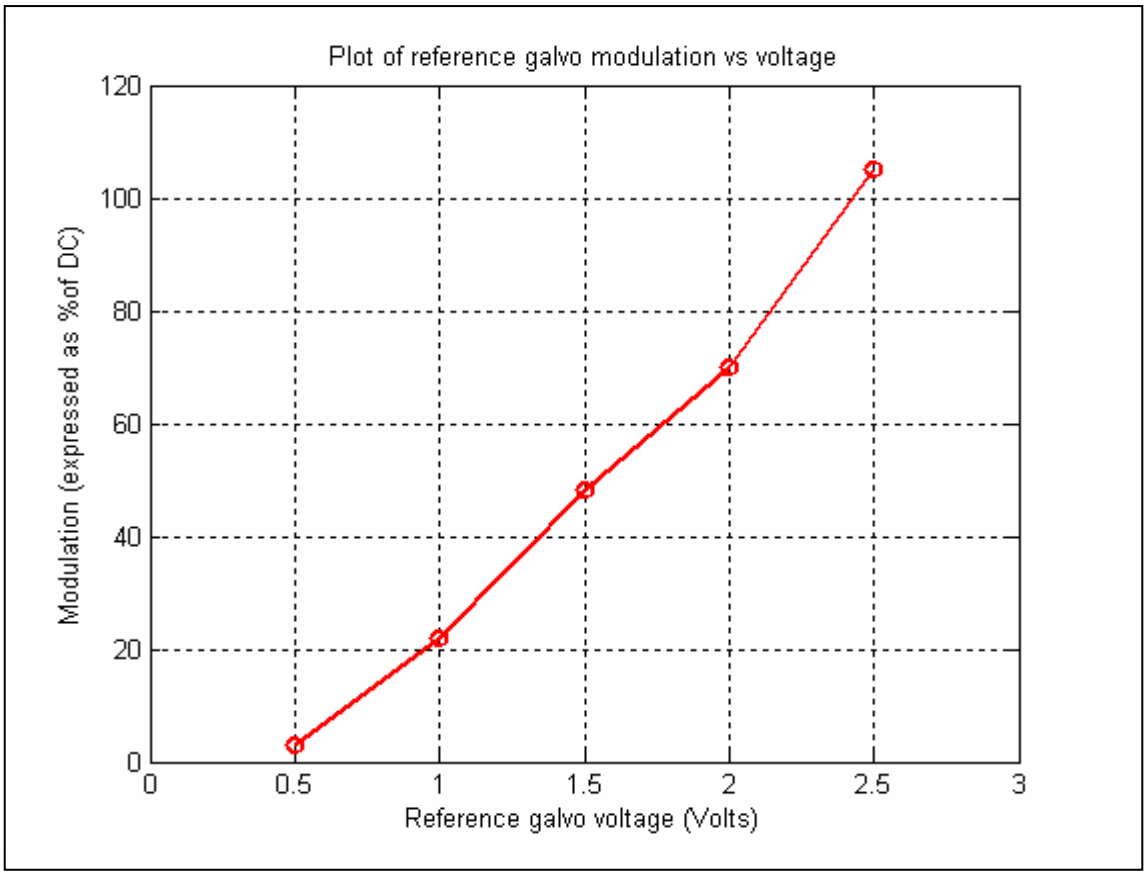

Figure 4.7: Reference galvo scan modulation dependence on input voltage.

Figure 4.6 and 4.7 show the depth of scan and modulation of scan as a function of input voltage to the galvo. Modulation of scan is defined as the ratio of peak to peak AC signal to the DC component of the signal. Figure 4.8 shows an increase in modulation with increase in depth of scan.

Figure 4.8: Reference galvo modulation dependence on depth of scan

The light coupled back from the delay line is also dependent on the dispersion. Dispersion compensation can be achieved by varying the grating to lens distance in the delay line. For a given spectrum, a dispersion compensated reference path (delay line) will result in a narrower coherence function fringe signal as compared to an uncompensated reference path (delay line) resulting in a narrow coherence length giving higher depth resolution. Figure 4.9 shows the difference in coherence length for a compensated and an uncompensated reference path.

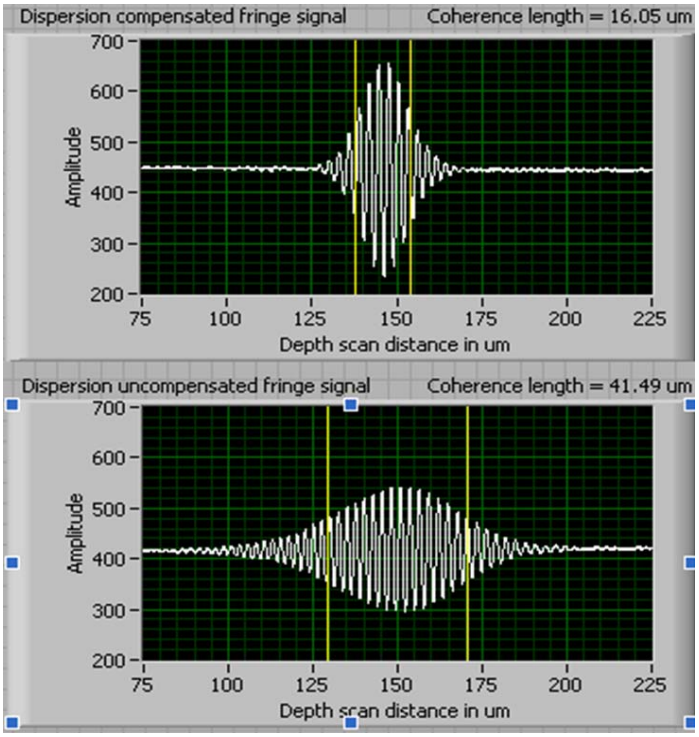

Figure 4.9: Difference in the coherence signal for an uncompensated delay line as compared to a compensated delay line.

4.4 Signal Analysis of the OCT system

It is unavoidable to exclude noise from any system. The factors that contribute towards noise in this OCT system are source bandwidth, intensity noise, receiver noise, and photon shot noise. This section explains the experiments that were conducted in order to estimate the SNR for the system. The analysis and contribution of the individual noise components is however beyond the scope of this thesis.

The Signal to noise of the system can be expressed as [31]

$$SNR = \frac{2\Re^2 P_{ref} P_{dut}}{4kT\,\Delta f / R_{eff} + 2q\Re P_{ref}\Delta f + (RIN)\Re^2 P_{ref}^2 \Delta f} \qquad 4.1$$

where R_{eff} and Δf are the effective noise resistance and the measurement bandwidth of the receiver. This result is under the assumption that the reference path power coupled is much than the sample path power coupled, which will be the case with most of the tissue samples. The first term in the denominator represents the receiver noise. Receiver noise is the noise in the detector. It consists of shot noise arising from the background light and dark current in the detector, thermal noise is due to the random thermal motion of electrons in the conductor and temperature noise dependent on the temperature fluctuations in the detector environment [18] [32]. The second term in the denominator is the photon shot noise due to the random arrival of photons at the detector [18] [3]. The third term in the denominator is the relative intensity noise. This intensity noise depends on the spectral bandwidth of the source and is related to the bandwidth as shown in equation 4.2 [31].

$$(RIN)\Re^2 P_{ref}^2 \Delta f \sim 2/\Delta\upsilon \qquad 4.2$$

For a Broad band source with bandwidth of the order of a few 100nm, the RIN becomes dominant for the reference path power of the order of a few microwatts. Beyond this point increasing the input power will not increase the signal to noise ratio of the system as both the numerator and the denominator increase at the same rate. SNR is seen to be the best when the power in the reference arm and the sample arm is the same [31].

The signal to noise analysis for the OCT system built was done for a mirror and a cover slip. Here the power from the sample path is much greater than the power from the reference power. The noise in the system was analyzed cumulatively and the noise

was assumed to be random in nature, its averaging over time should be zero was the basis for this analysis. The receiver signal can thus be defined as shown in equation 4.3.

$$I_{measured} = I_{signal} + I_{noise} \tag{4.3}$$

noise was measured as root mean square (rms) standard deviation σ or the mean square variance σ^2 [33]The noise of the system was defined as shown in equation 4.4.

$$\sigma_i^2 = \frac{1}{n}\sum_{i=1}^{n}\left(x_i - \bar{x}\right)^2 \tag{4.4}$$

where n is the number of instances for noise evaluation and x_i is the detector output at i^{th} instance. The SNR ratio for the system was defined as shown in equation 4.5

$$SNR = 10\log\left(\frac{I_{s\max}^2}{\sigma^2}\right) \tag{4.5}$$

The I_{smax} is the maximum signal detected for the sample. The experiment was done for varying intensities of signal input to the interferometer for mirror and cover slip. The gain to the detector was also varied. Mirror as a sample was chosen to satisfy the condition of power in the sample path being much greater than the reference path power. It is seen from the graph that the SNR stops increasing with increase in input power to the interferometer after a certain power in the sample path. Cover slip was chosen to satisfy the condition of reference path power being comparable to sample path power. The SNR for the system for a condition where reference path power is comparable to the sample path power is 61 dB. (SNR graphs are shown in Appendix C).The signal to noise ratio was experimentally determined using a 16 bit DAC interface thus the SNR analysis was limited by the SNR of the DAC card 96.32 dB.

Since the 16 bit card had a lower sampling rate, a faster card was used to data acquisition for the OCT system. A compromise had to be made with the SNR of the card and the acquisition rate for this system.

CHAPTER 5

RESULTS AND DISCUSSION

All the images are taken with a broad band and narrow band source. The comparison of reconstructed narrow band and the broad band images show a difference in the depth resolution of the images. This TD-OCT system is capable of imaging samples at a resolution of 5μm in depth and close to about 2μm laterally.

5.1 Mirror

Mirror, sample with just one surface. Light falling on the mirror gets reflected form the surface of the mirror. While scanning in depth we see a single bright band. The thickness of this band depends on the coherence length of the fringe. Figure 5.1 shows the depth scan image of mirror for a broadband and a narrow band source. As can be seen from the images in figure 5.1, the single surface of the mirror is broader for a narrow band source and with a thinner for a broad band source.

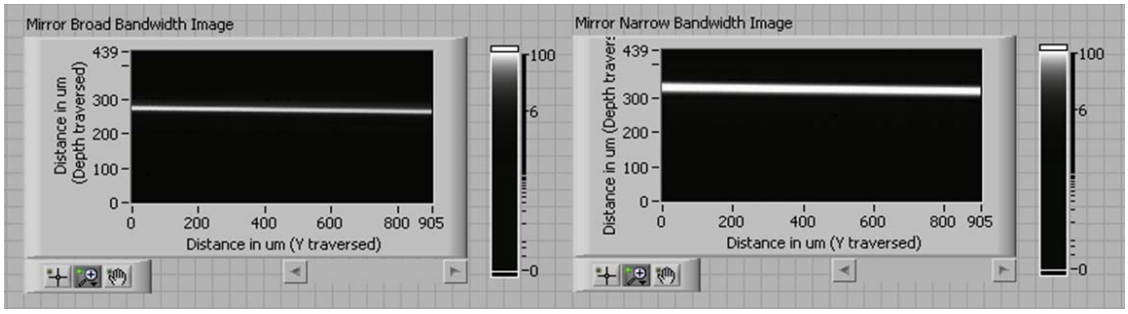

Figure 5.1 Depth scan image of a mirror with narrowband and broadband source

5.2 Cover slip

A depth scan OCT image of a coverslip will show two surfaces for the cover slip. The distance between the two lines gives us the optical thickness of the cover slip. The thickness of the lines showing the cover slip surfaces depends on the bandwidth of the source. Figure 5.2 shows the edges of a cover slip as seen by an OCT depth scan.

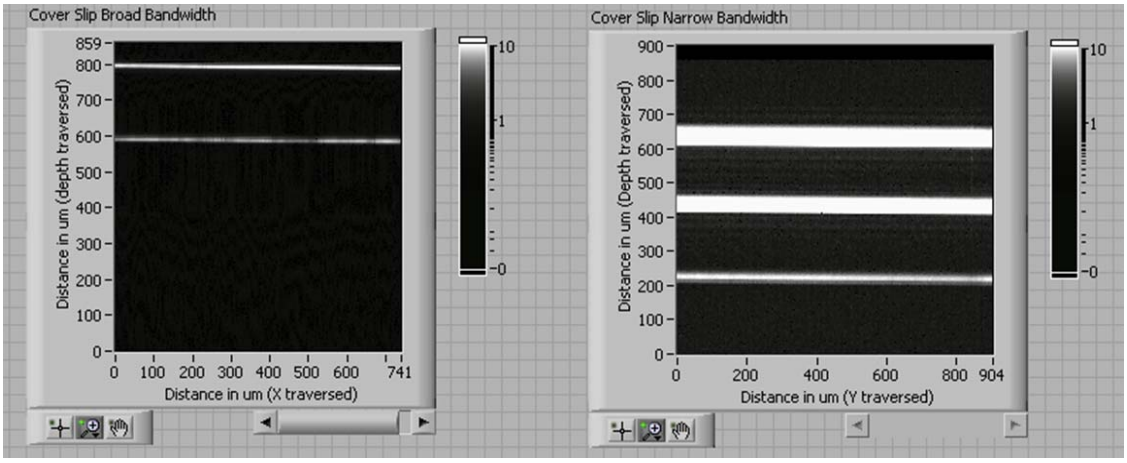

Figure 5.2: Depth scan image of a cover slip with broadband and narrowband source.

Image of the cover slip with narrow band source shows three bands. First two bands as can be seen are the top and bottom surface of the cover slip. Third band is due to multiple reflection of light between the two surfaces of the cover slip. The image clearly shows the advantages of imaging with the broad band source and the capabilities of this OCT system to image using broadband source.

5.3 Onion Images

Onion cells are very large, in the order of a few hundred microns. Figure 5.3 shows the OCT images of onion obtained using Broad band and narrow band source. There is a clear distinction in the image obtained using Broad band source. The cells are clearer and the resolution is higher while imaging with a broad band source.

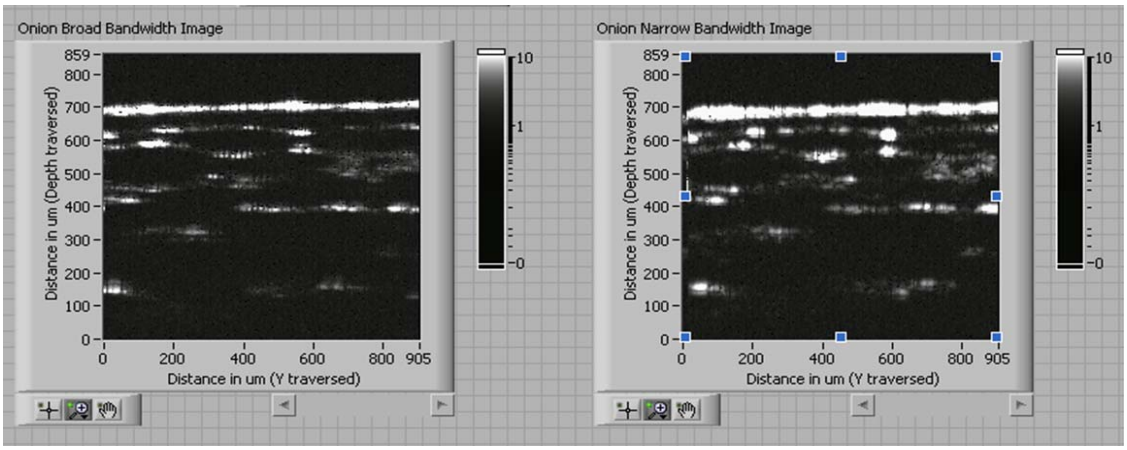

Figure 5.3 Depth scan image of an onion with broadband and narrowband source.

All the images above emphasize on use of a broad band source for OCT imaging. The resolution of an OCT image can be increased by reducing the band width of the source.

5.4 Tissue Images

The images in figure 5.4 – 5.8 are acquired from a human volunteer's finger. The images comprise 200 axial and 5000 traverse pixels. Focal point of the imaging lens was placed in the middle of the depth range. Images were plotted using logarithmic and inverse logarithmic grey scale.

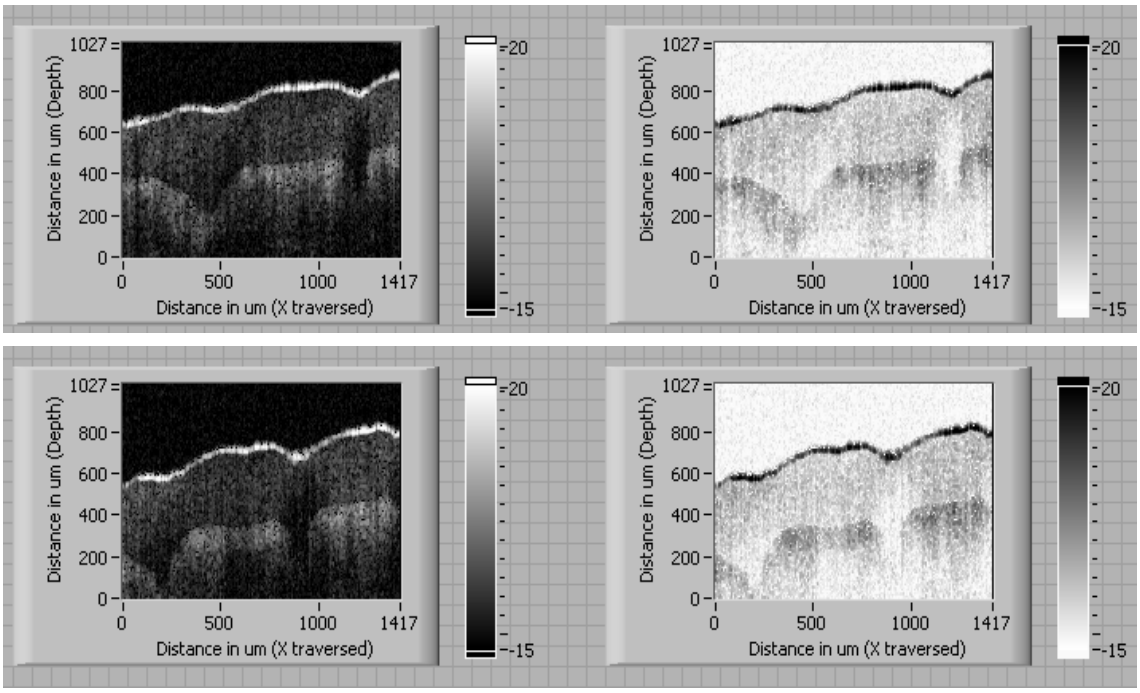

Figure 5.4: Images of the ventral portion of a human finger close to the finger joints.

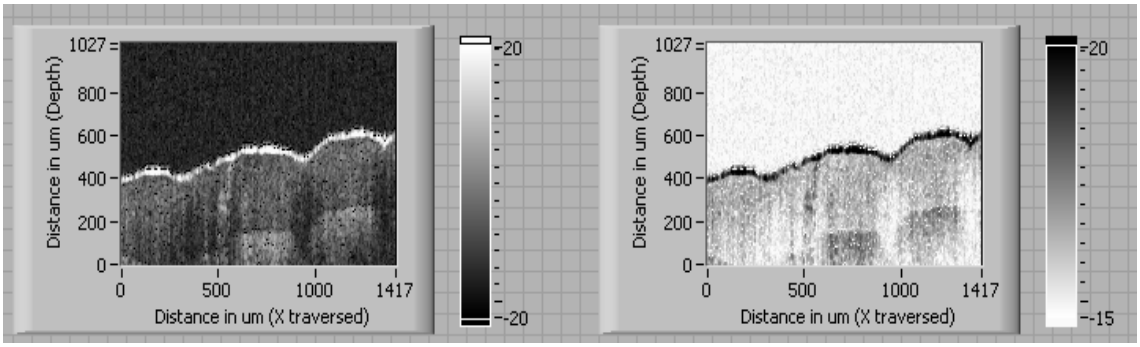

Figure 5.5: Images of the ventral portion of human finger. (Finger tip)

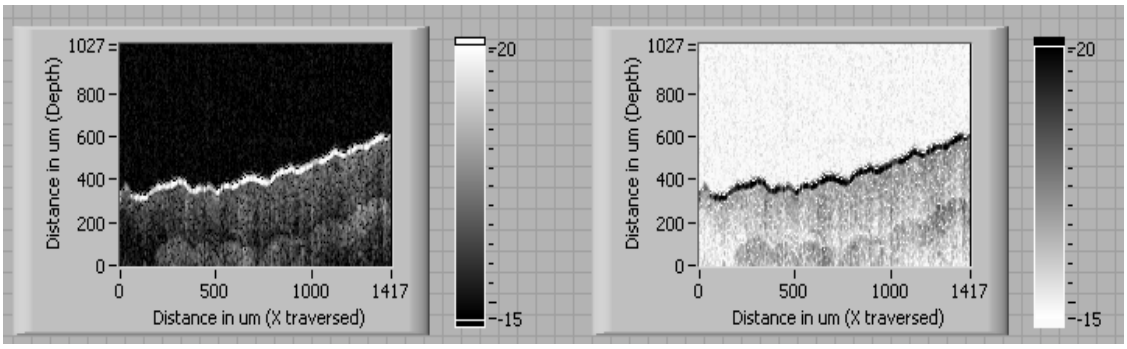

Figure 5.6: Images of the dorsal portion of a human finger.

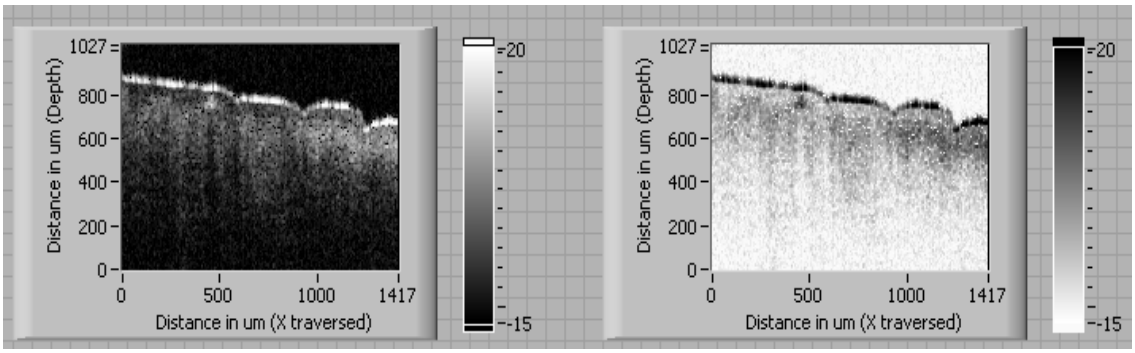

Figure 5.7: Images of dorsal portion of human finger. (Right side of the image shows injured tissue on the volunteer's finger).

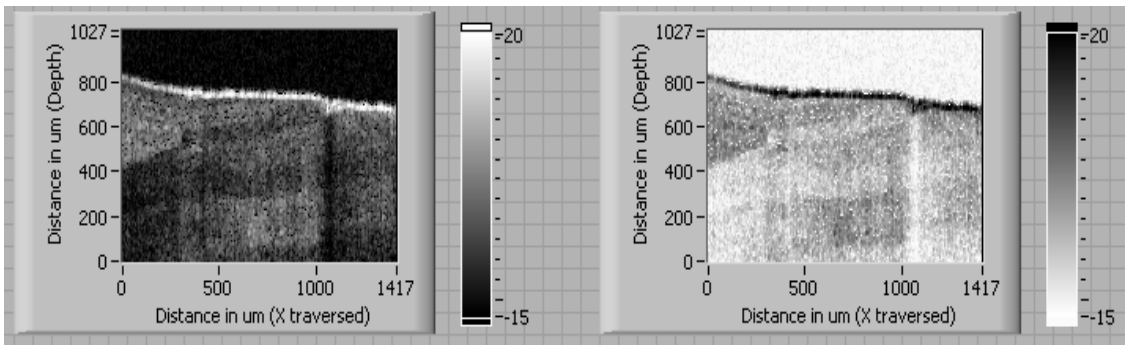

Figure 5.8: Images of the cuticle (Human Finger).

CHAPTER 6

CONCLUSION

This TD-OCT system was seen to be capable of imaging samples at a resolution of 7μm in depth and close to about 10μm laterally, fulfilling the objectives of the thesis. The system is also calibrated and integrated with a DIC microscope as shown in the figure 6.1.

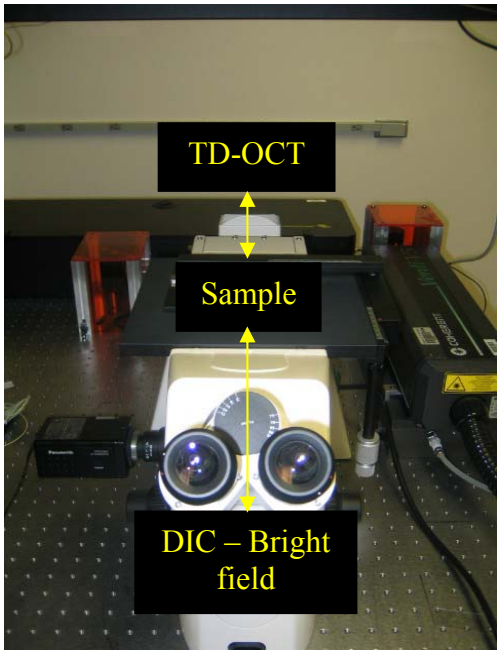

Figure 6.1: TD-OCT system integrated with the DIC microscope block diagram.

The OCT system was built as a part of a virtual biopsy imaging workstation. As shown in the figure 6.1. It also has ports for future expansion of the workstation with imaging modalities such as multi photon imaging and spectral imaging. The TD-OCT system can also be used for spectral domain OCT.

Currently the TD-OCT system is capable of acquiring and displaying images at 2 frames per second which can be improved by running the galvos faster. The galvo being an electro mechanical device, it is difficult to go faster than a 400 Hz for displacements greater than a few mm peak to peak.

The image resolution of the system is also dependent on the number of depth scans in fixed time duration. This can be improved by running the galvos faster. Even though the galvos are capable of running at 400 Hz, the computer system configuration does not allow acquisition of enough number of data points and process them at the same time for frequencies greater than 200 Hz. This limitation can be taken care off by either increasing the random access memory on the computer or by not displaying the image with the acquisition module. The data can be saved and viewed at a later time.

System can also be enhanced by incorporating objective lenses of higher magnification. All the Images obtained were at a 10x resolution and the focal length of the objective used was 25.4mm. This limits the axial resolution if the system.

Overall the enhancements listed will improve the performance of the system.

APPENDIX A

BEAM SPOT SIZE CALCULATION

Beam spot size calculation is based on Gaussian beam optics equations. From equation 1.5

$$\Delta x = \frac{4\lambda}{\pi}\left(\frac{f}{d}\right)$$

where

d is the beam diameter at the the lens (collimated beam diameter) = 2.4 mm

λ is the center wavelength. = 800 nm

f is the focal length of the lens. =25.4 mm

Δx is the spot size of the beam at the sample was calculated to be =10.78 μm

APPENDIX B

DETECTOR SPECIFICATION AND GRAPHS

PDA520 Operating Manual
High Precision Amplified Silicon Detector

Description:

The PDA520 is a high precision, high accuracy, low noise, and switchable-gain silicon detector designed for detection of light in the wavelength range of 400 to 1100nm. A three-position rotary switch allows the user to vary the gain in 10 dB steps. A buffered output drives a 50Ω load impedance up to 5 volt. The PDA520 housing includes a removable threaded coupler that is compatible with any number of Thorlabs 1" threaded accessories. This allows convenient mounting of external optics, light filters, apertures, as well as providing an easy mounting mechanism using the Thorlabs cage assembly accessories.

The PDA520 has an 8-32 tapped mounting hole with a 0.25" mounting depth and includes a 120VAC 50-60Hz power supply. The PDA520-EC has an M4 tapped mounting hole and includes a 230VAC 50-60Hz power supply.

Specifications:

Detector	
Detector	Silicon
Active Area	10 x 10 mm
Aperture Diameter	ϕ0.348" (ϕ8.8mm)
Response Range	400 to 1100 nm
Peak Response	0.65 A/W @ 980 nm
Damage Threshold	1W/cm² CW
Output Voltage (50Ω)[1]	0 to 4.5V(min) 0 to 5V (typ)
Output voltage (HI-Z)[1,5]	0 to 9V(min) 0 to 10V (typ)
Output Impedance[1]	50Ω
Load Impedance[1,5]	50Ω / HI -Z
Max Output Current	100mA
Gain Steps	0, 10, 20dB
Gain Switch	3-Pos Rotary
On / Off Switch	Toggle
Output	BNC
Optical Head Size[2]	ϕ1.425" x 1.45"
Weight	60 grams
Accessories	SM1T1 Coupler
Operating Temp	10 to 40°C
Storage Temp	-20 to 70°C
Power Supply	Linear AC - DC
Input Power	100-120VAC, 50-60Hz, 5W (220-240VAC –EC)

Performance	min	typical	max
0 dB Setting			
Transimpedance Gain[1]		1.0×10^4 V/A	
Trans. Gain (50Ω)[1,5]		5.0×10^3 V/A	
Gain Error[6]		+/- 0.1%	+/- 0.12%
NEP (980nm, 0dB)[3]		$<3 \times 10^{-13}$ W/√Hz	
Noise (RMS)[3]		<0.1 mV	
Offset[3]	-1 mV	+/- 0.1mV	1 mV
Bandwidth[3,4]		250kHz	
10 dB Setting			
Transimpedance Gain[1]		1.0×10^5 V/A	
Trans. Gain (50Ω)[1,5]		5×10^4 V/A	
Gain Error[6]		+/- 0.12%	+/- 0.15%
NEP (980nm, 10dB)[3]		5.4×10^{-12} W/√Hz	
Noise (RMS)[3]		0.175 mV	0.2 mV
Offset[3]	-5 mV	+/- 1mV	5 mV
Bandwidth[3,4]		250kHz	
20 dB Setting			
Transimpedance Gain[1]		1.0×10^6 V/A	
Trans. Gain (50Ω)[1,5]		5×10^5 V/A	
Gain Error[6]		+/- 0.14%	+/- 0.3%
NEP (980nm, 20dB)[3]		4.6×10^{-12} W/√Hz	
Noise (RMS)[3]		1.2 mV	1.5 mV
Offset[3]	-20 mV		20 mV
Bandwidth[3,4]		160kHz	

Note 1: The PDA520 has a 50Ω terminating resistor in series with amplifier output. This forms a voltage divider with any load impedance (e.g. 50Ω load divides signal in half).

2: Newer PDA's have a smaller package diameter to easily fit into Thorlabs cage plate assemblies. Also note that the length includes the SM1T1 mounting adapter and the BNC / power switch.

3: Test performed with a 50Ω terminator and 6' coax cable.

4: See 'PDA520 Bandwidth' curve for frequency response.

5. Definition of HI-Z: High impedance. Refers to an oscilloscope or measurement device input. Actual impedance values should be 1MΩ or higher. Lower values will create a voltage divider with the output 50Ω impedance and will cause larger gain errors than what is specified.

6. The gain error does not apply to the 50Ω load since the user installed output terminating resistor will probably have a resistance tolerance greater than the gain errors above. Also note that the 50Ω output series resistance is 49.9Ω +/- 1%. This will also factor into gain error when using a 50Ω load.

Figure B1: Specification sheet for PDA520 silicon detector

Graphical Data:

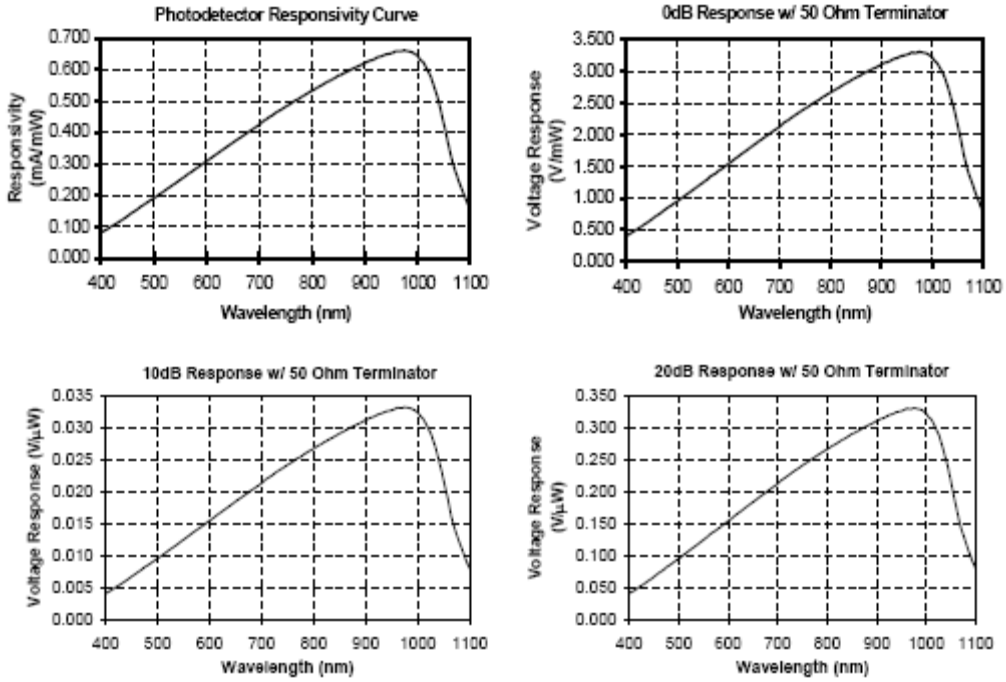

Figure B2: PDA520 responsivity curve at varying electrical gain settings

APPENDIX C

SIGNAL TO NOISE RATIO

Signal to noise analysis

The SNR analysis was done for both mirror and cover slip. The SNR was evaluated for varying electrical gain.

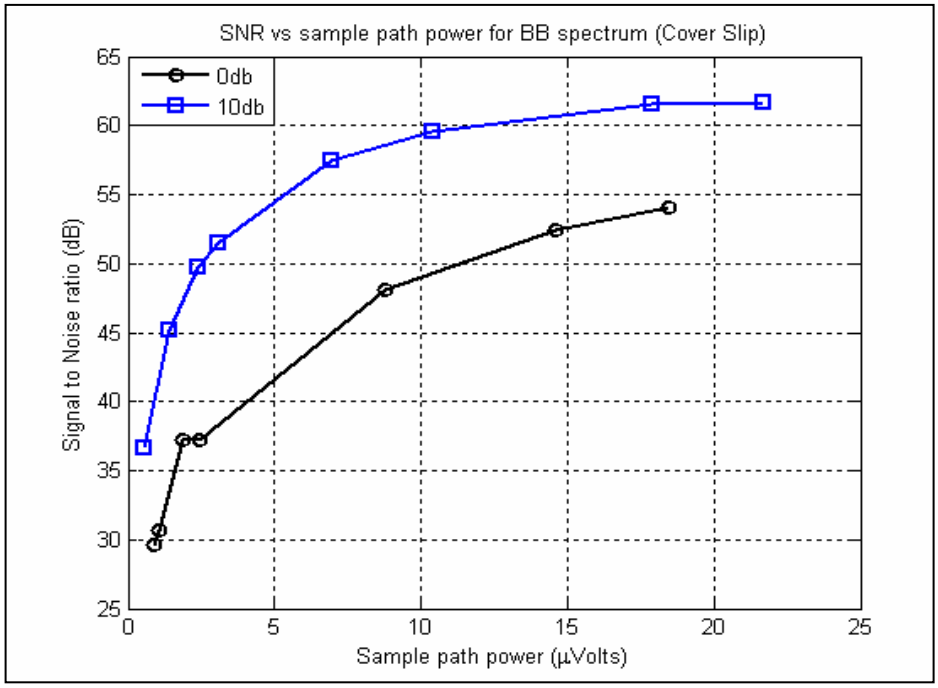

Figure C1: SNR of the system plotted against the Sample path power for a broadband spectrum with cover slip as a sample.

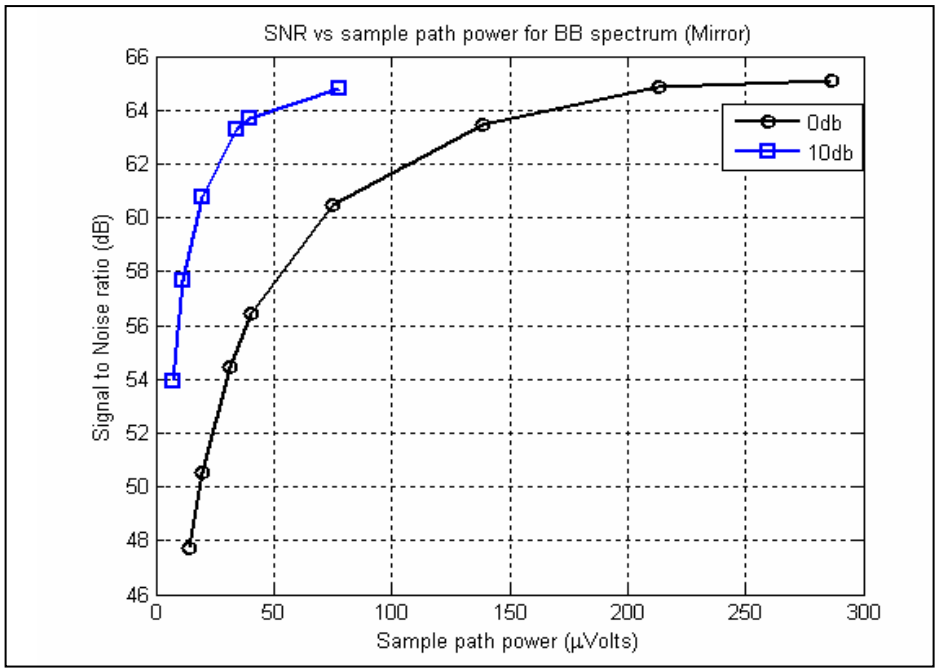

Figure C2: SNR of the system plotted against the Sample path power for a broadband spectrum with mirror as a sample.

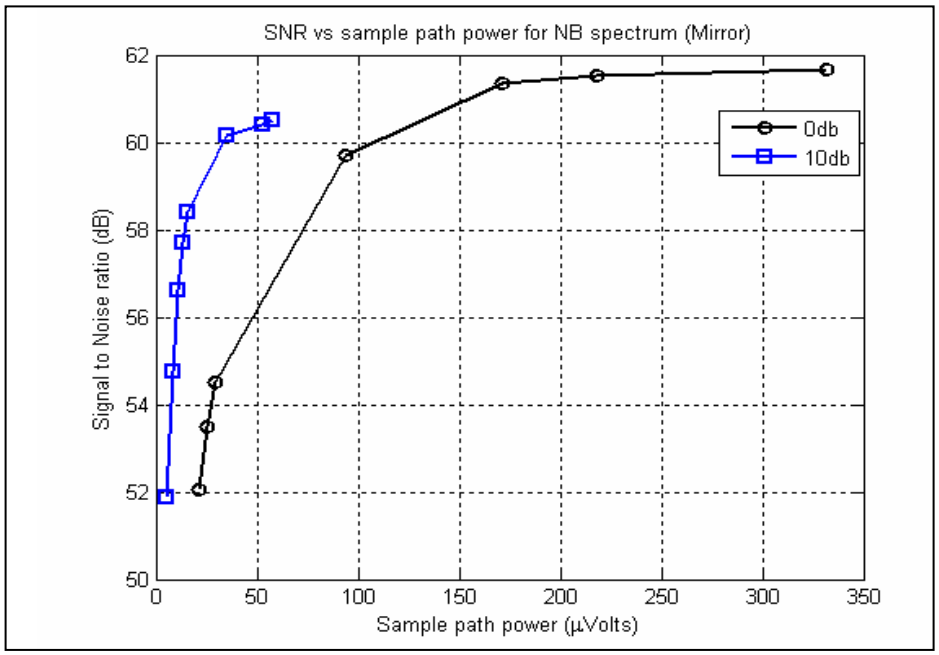

Figure C3: SNR of the system plotted against the Sample path power for a narrow band spectrum with mirror as a sample.

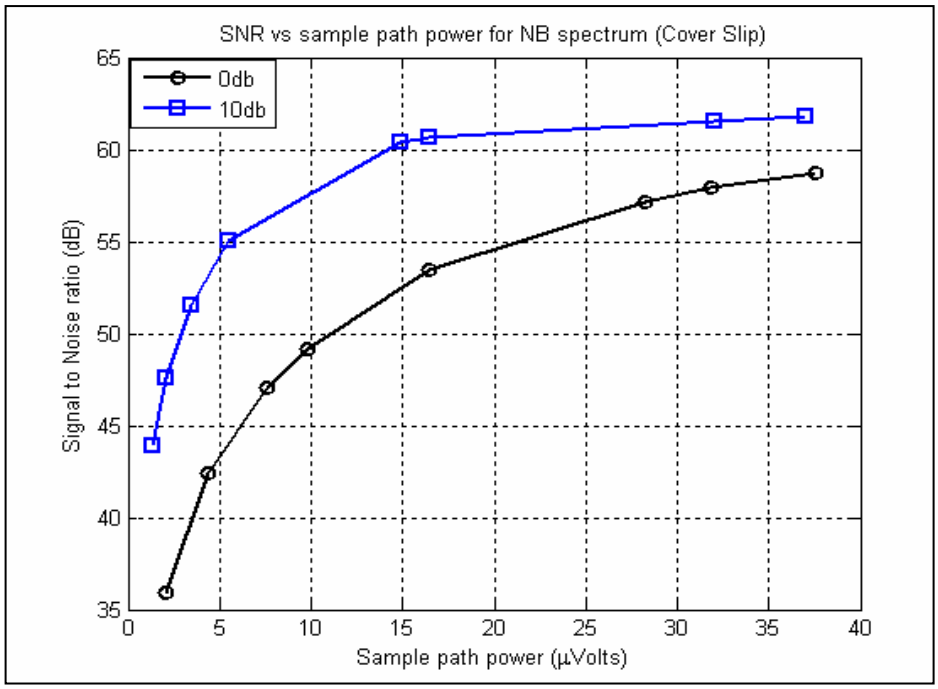

Figure C4: SNR of the system plotted against the Sample path power for a narrow band spectrum with cover slip as a sample.

REFERENCES

[1] Optical Coherence Tomography (OCT): A Review- Joseph M. Schmitt. IEEE J. of selected topics in quantum electronics, 5(4), (July/August 1999)

[2] Optical Coherence Tomography-Principles and application- A F Fercher, W Drexler, C K Hitzenberger and T Lasser Journal Biomed. Opt. 1, 157-173 (1996)

[3] Detection and Diagnosis of Oral Neoplasia with Confocal Microscopy and Optical Coherence Microscopy. PhD Desertation , University of Austin, 2003.

[4] C. Toth, D. Narayan, S. Boppart, M. Hee, J. Fujimoto, R. Birngruber, C. Cain, C. DiCarlo, and W. Roach, "A comparison of retinal morphology viewed by optical coherence tomography and by light microscopy," Archives of Ophthalmology, vol. 115, pp. 1425-1428, 1997.

[5] C. D. DiCarlo, W. P. Roach, D. A. Gagliano, S. A. Boppart, D. X. Hammer, A. B. Cox, and J. G. Fujimoto, "Comparison of optical coherence tomography imaging of cataracts with histopathology," Journal of Biomedical Optics, vol. 4, pp. 450, 1999.

[6] M. G. Ducros, J. F. de Boer, H.-E. H. Huang, L. C. Chao, Z. Chen, J. S. Nelson, T. E. Milner, and H. G. Rylander, III, "Polarization sensitive optical coherence tomography of the rabbit eye," IEEE Journal of Selected Topics in Quantum Electronics, vol. 5, pp. 1159-1167, 1999.

[7] M. R. Hee, J. A. Izatt, E. A. Swanson, D. Huang, J. S. Schuman, C. P. Lin, C. A. Puliafito, and J. G. Fujimoto, "Optical coherence tomograph for ophthalmic imaging," IEEE Engineering in Medicine and Biology, pp. 67-76, 1995.

[8] V. Kamensky, F. I. Feldchtein, V. M. Gelikonov, L. Snopova, S. Muraviov, A. Malyshev, N. Bityurin, and A. M. Sergeev, "In situ monitoring of laser modification process in human cataractous lens and porcine cornea using coherence tomography," Journal of Biomedical Optics, vol. 4, pp. 137-143, 1999

[9] Detection of tumorigenesis in urinary bladder with optical coherence tomography: optical characterization of morphological changes.-T. –Q. Xie, M. L. Zeidl, Y. –T. Pan Optical Express 10(24), 1431-1443, (10-October 2002)

[10] In vivo endoscopic OCT imaging of precancer and cancer states of human mucosa A. M. Sergeev, V. M. Gelikonov, G. V. Gelikonov, F. I. Feldchtein, R. V. Kuranov, N. D. Gladkova N. M. Shakhova, L. B. Snopova, A. V. ShakhovNizhny I. A. Kuznetzova, A. N. Denisenko, V. V. Pochinko, Yu. P. Chumakov, O. S. Streltzova

[11] In Vivo Optical Coherence Tomography for the Diagnosis of Oral Malignancy Petra Wilder-Smith, DDS, PhD,1* Woong-Gyu Jung, MSc,1 Matthew Brenner, MD,2 Kathryn Osann, PhD,2 Hamza Beydoun, BS,1 Diana Messadi, DDS, DMSc,3 and Zhongping Chen, PhD

[12] Endoscopic optical coherence tomography with a modified microelectromechanical systems mirror for detection of bladder cancers Tuqiang Xie, Huikai Xie, Gary K. Fedder, and Yingtian Pan

[13] OPTICS LETTERS / Vol. 28, No. 8 / April 15, 2003 Electrostatic micromachine scanning mirror for optical coherence tomography J. M. Zara, S. Yazdanfar, K. D. Rao, J. A. Izatt, and S. W. Smith

[14] October 1, 2004 / Vol. 29, No. 19 / OPTICS LETTERS 2261 Micromotor endoscope catheter for invivo, ultrahigh-resolution optical coherence tomography P. R. Herz, Y. Chen, A. D. Aguirre, K. Schneider, P. Hsiung, and J. G. Fujimoto

[15] Enhancing early bladder cancer detection with fluorescence-guided endoscopic optical coherence tomography Y. T. Pan and T. Q. Xie, C. W. Du, S. Bastacky, S. Meyers, and M. L. Zeidel

[16] Optical coherence tomography: feasibility for basic research and image-guided surgery of breast cancer Stephen A. Boppart1, Wei Luo2, Daniel L. Marks2, and Keith W. Singletary

[17] Effect of target biological tissues and choice of light source on penetration depth and resolution in optical coherence tomography.- Ann W. Sainter, Terry A. King, Mark R. Dickinson Journal of biomedical optics, 9(1), 193-199 (January/Feburary 2004)

[18] Optical Coherence Tomography: System Design and Noise Analysis Overview - Michael H. Frosz, Michael Juhl, Modrten H. Lang Risø National Laboratory, University of Denmark. ISBN 87—550—2904—3 (Internet)

[19] Optical coherence tomography and microscopy in gastrointestinal tissues.- J. A. Izatt, M. D. Kulkarni, H. Wang, K. Kobayashi and M. V. Sivak J. Selec. Top. Quant. Elec. 2(4), 1017-1028 (1996).

[20] Advances in broad bandwidth light sources for ultra high resolution optical coherence tomography.- A Unterhuber, B Povazay, K Bizheva, B Hermann, H Sattmann,A Stingl, T Le, M Seefeld, R Menzel, M Preusser, H Budka, Ch Schubert, H Reitsamer, P K Ahnelt, J E Morgan, A Cowey and W Drexler. Phys. Med. Biol. 49, 1235-1246 (2004)

[21]L. Thrane, Optical Coherence Tomography: Modeling and Applications, PhD thesis, Risø-R-1217(EN), 2000.

[22] The frequency-domain delay line in Optical coherence Tomography: Design, Capabilities and limitations.-David D. Sampson, Andrei V. Zvyagin, Elwyn D J. Smith, Ian D. Watson, Julian J. Armstrong, K. K. M. B. Dilusha Silva

[23] 400-Hz mechanical scanning optical delay line - K. F. Kwong, D. Yankelevich, K. C. Chu, J. P. Heritage, A. Dienes. Opt. Lett., 18, 558-560 (1993)

[24] In-vivo video rate optical coherence tomography.- Andrew M. Rollins, Manish D. Kulkarni, Siavash Yazdanfar, Rujchai Ung-arunyawee, Joseph A. Izatt Optical Express 3(6), 219-229 (14-September 1998)

[25] Delay and dispersion characteristics of a frequency-domain optical delay line for scanning interferometry.-Andrei V. Zyvagin, Elwyn D. J. Smith, David. D. Sampson
J. Opt. Soc. Am., 20(2), 333-341, (February 2003)

[26] Interferometer for optical coherence tomography.- Christoph Hauger, Marco Wörz, Thomas Hellmuth Applied Optics, 42(19), 3896-3902, (1 July 2003)

[27] Three dimentional OCT images from retina and skin -Adrian Gh. Podoleanu, John A. Rogers, David A. Jackson Optics Express 7(9), 292-298, (23 October 2000)

[28] Shaping and analysis of picosecond light pulses -C. Froehly, B. Colombeau, M. Vampouille Progress in optics XX, (E. Wolf, Ed.), 63-153, (1983)

[29] High speed phase- and group-delay scanning with a grating based phase control delay line-G. J. Tearney, B. E. Boum, J. G. Fujimoto Opt. Lett. 22, 1811-1813 (1997)

[30] A simple intensity noise reduction technique optical low-coherence reflectometry. -W. V. Sorin, D. M. Baney IEEE Photonics Technology Letters VOL. 4, No.2, Dec 1992

[31] H. W. Ott, Noise Reduction Techniques in Electronic Systems John Wiley & Sons, Inc., 2. edition, 1988, ISBN 0-471-85068-3.

[32] A. Rollins and J. A. Izatt, SNR Analysis of Conventional and Optimal Fiber- Optic Low-Coherence Interferometer Topologies, Proceedings of SPIE 3915, 60—67 (2000).

[33] F. Grum and R. J. Becherer, Radiometry, volume 1 of Optical Radiation Measurements, Academic Press, 1979, ISBN 0-12-304901 (v. 1).

BIOGRAPHICAL INFORMATION

Kapil Bharati Langer was born in Srinagar, province of Jammu and Kashmir (J&K), India. Son of Kiran and Kumud Langer, he grew up traveling all over the Indian subcontinent as his father worked away from his native land of J&K. He graduated high school from Don Bosco, Delhi, India, and continued to pursue his BE in Instrumentation and Electronics engineering from R.V.College of Engineering, Bangalore, India.

Before graduating as a bachelor of engineering he was selected by WIPRO Technologies to work with their embedded systems group providing device driver support for printers and scanners. He served WIPRO tech. for about two years before deciding to pursue further studies.

His quest for learning new modalities and applications pertaining to Instrumentation and Electronics lured him into MS in Biomedical Engineering at the University of Texas at Arlington. He worked several projects to keep in touch with his skills as a programmer and an electronics engineer. He went on to work with a new faculty member assisting him in his optical lab setup and also developing an optical imaging modality to provide high resolution images of tissue samples.